UNIVERSITY OF CALIFORNIA, SAN DIEGO

Infrared probe of electrostatic doping in novel materials

A dissertation submitted in partial satisfaction of the
requirements for the degree Doctor of Philosophy

in

Physics

by

Zhiqiang Li

Committee in charge:

Professor Dimitri N. Basov, Chair
Professor Massimiliano Di Ventra
Professor Michael M. Fogler
Professor Andrew C. Kummel
Doctor Michael C. Martin
Professor William C. Trogler

2008

The dissertation of Zhiqiang Li is approved, and it is acceptable in quality and form for publication on microfilm and electronically:

_____

_____

_____

_____

_____

_____

Chair

University of California, San Diego

2008

To my family

TABLE OF CONTENTS

LIST OF FIGURES

LIST OF TABLES

ACKNOWLEDGEMENTS

First and foremost I would like to thank my advisor Professor Dimitri Basov. I have never worked so closely with someone for such a long time before, which turns out to be wonderful and fruitful. Dimitri's wisdom and illuminating guidance will benefit me for my whole life. I am very fortunate to have the opportunity to work with him.

I am grateful to all my collaborators for their critical contributions to my work and this dissertation. It has been a great pleasure working with them.

I thank the former and current members of the Basov lab for their numerous help.

Finally, I would like to dedicate this thesis to my family.

Chapter 2 contains materials in Z.Q. Li, G.M. Wang, K.J. Mikolaitis, D.Moses, A. J. Heeger, and D.N. Basov, "*An infrared probe of tunable dielectrics in metal-oxide-semiconductor structures*", Appl. Phys. Lett. 86, 223506 (2005). Chapter 3 contains materials in Z.Q. Li, G.M. Wang, N. Sai, D. Moses, M.C. Martin, M. Di Ventra, A.J. Heeger, and D.N. Basov, "*Infrared Imaging of the Nanometer-Thick Accumulation Layer in Organic Field-Effect Transistors*", Nano Letters 6, 224 (2006). Chapter 4 contains materials in Z.Q. Li, V. Podzorov, N. Sai, M.C. Martin, M.E. Gershenson, M. Di Ventra and D.N. Basov, "*Light Quasiparticles Dominate Electronic Transport in Molecular Crystal Field-Effect Transistors*", Phys. Rev. Lett. 99, 016403 (2007). Chapter 5 contains materials in Z.Q. Li, E.A. Henriksen, Z. Jiang, Z. Hao, M.C. Martin, P. Kim, H.L. Stormer, and D.N. Basov, "*Dirac charge dynamics in graphene by infrared spectroscopy*", Nature Physics 4, 532 (2008). Chapter 6 contains materials in

Z.Q. Li, E.A. Henriksen, Z. Jiang, Z. Hao, M.C. Martin, P. Kim, H.L. Stormer, and D.N. Basov, "*Band structure asymmetry of bilayer graphene revealed by infrared spectroscopy*", arXiv:0807.3776 (2008), which was submitted and posted online. Chapter 7 contains materials in Z.Q. Li, S.-W. Tsai, W.J. Padilla, S.V. Dordevic, K.S. Burch, Y.J. Wang, and D.N. Basov, "*Infrared probe of the anomalous magnetotransport of highly oriented pyrolytic graphite in the extreme quantum limit*", Phys. Rev. B 74, 195404 (2006). The dissertation author was the primary investigator and author of all these papers. The coauthors of these papers all contribute to the studies describe in the corresponding chapter.

VITA

2002 B.S. Physics, Peking University, P.R. China

2002-2003 Teaching assistant, University of California, San Diego

2003-2008 Graduate student researcher, University of California, San Diego

2004 M.S. Physics, University of California, San Diego

2008 Ph.D. Physics, University of California, San Diego

PUBLICATIONS

1: Z.Q. Li, E.A. Henriksen, Z. Jiang, Z. Hao, M.C. Martin, P. Kim, H.L. Stormer, and D.N. Basov, "*Band structure asymmetry of bilayer graphene revealed by infrared spectroscopy*", arXiv:0807.3776. (2008).

2: Z.Q. Li, E.A. Henriksen, Z. Jiang, Z. Hao, M.C. Martin, P. Kim, H.L. Stormer, and D.N. Basov, "*Dirac charge dynamics in graphene by infrared spectroscopy*", Nature Physics 4, 532 (2008).

3: Z.Q. Li, V. Podzorov, N. Sai, M.C. Martin, M.E. Gershenson, M. Di Ventra and D.N. Basov, "*Light Quasiparticles Dominate Electronic Transport in Molecular Crystal Field-Effect Transistors*", Phys. Rev. Lett. 99, 016403 (2007).

4: Z.Q. Li, G.M. Wang, N. Sai, D. Moses, M.C. Martin, M. Di Ventra, A.J. Heeger, and D.N. Basov, "*Infrared Imaging of the Nanometer-Thick Accumulation Layer in Organic Field-Effect Transistors*", Nano Letters 6, 224 (2006).

5: Z.Q. Li, S.-W. Tsai, W.J. Padilla, S.V. Dordevic, K.S. Burch, Y.J. Wang, and D.N. Basov, "*Infrared probe of the anomalous magnetotransport of highly oriented pyrolytic graphite in the extreme quantum limit*", Phys. Rev. B 74, 195404 (2006).

6: Z.Q. Li, G.M. Wang, K.J. Mikolaitis, D.Moses, A. J. Heeger, and D.N. Basov, "*An infrared probe of tunable dielectrics in metal-oxide-semiconductor structures*", Appl. Phys. Lett. 86, 223506 (2005).

7: A. D. LaForge, W. J. Padilla, K. S. Burch, Z. Q. Li, A. A. Schafgans, Kouji Segawa, Yoichi Ando, and D. N. Basov, "*Sum Rules and Interlayer Infrared Response of the High Temperature $YBa_2Cu_3O_y$ Superconductor in an External Magnetic Field*", Phys. Rev. Lett. 101, 097008 (2008).

8: M. M. Qazilbash, Z. Q. Li, V. Podzorov, M. Brehm, F. Keilmann, B. G. Chae, H. T. Kim, and D. N. Basov, "*Electrostatic modification of infrared response in gated structures based on VO_2*", Appl. Phys. Lett. **92**, 241906 (2008).

9: A.D. Meyertholen, Z.Q. Li, D.N. Basov, M.M. Fogler, M.C. Martin, G.M. Wang, A.S. Dhoot, D. Moses, and A.J. Heeger, "*Concentration-dependent mobility in organic field-effect transistors probed by infrared spectromicroscopy of the charge density profile*", Appl. Phys. Lett. **90**, 222108 (2007).

10: N. Sai, Z.Q. Li, M.C. Martin, D.N. Basov, and M. Di Ventra, "*Electronic excitations and metal-insulator transition in poly(3-hexylthiophene) organic field-effect transistors*", Phys. Rev. B 75, 045307 (2007).

11. A.D. LaForge, W.J. Padilla, K.S. Burch, Z.Q. Li, S.V. Dordevic, Kouji Segawa, Yoichi Ando, and D.N. Basov, "*Interlayer electrodynamics and unconventional vortex state in $YBa_2Cu_3O_y$*," Phys. Rev. B 76, 054525 (2007).

12: Y.S. Lee, Z.Q. Li, W.J. Padilla, S.V. Dordevic, C.C. Homes, K. Segawa, Y. Ando, and D.N. Basov, "*Strong-coupling effects in cuprate high-T_c superconductors by magneto-optical studies*", Phys. Rev. B 72, 172511 (2005).

13: Y.S. Lee, K. Segawa, Z.Q. Li, W.J. Padilla, M. Dumm, S.V. Dordevic, C.C. Homes, Y. Ando, and D.N. Basov, "*Electrodynamics of the nodal metal state in weakly doped high-T_c cuprates*", Phys. Rev. B 72, 054529 (2005).

14: W.J. Padilla, Z.Q. Li, K.S. Burch, Y.S. Lee, K.J. Mikolaitis, and D.N. Basov, "*Broadband multi-interferometer spectroscopy in high magnetic field from THz to visible",* Review of Scientific Instruments 75, 4710 (2004).

FIELDS OF STUDY

Major Field: Phyics

Infrared Spectroscopy of Electrostatic Doping in Novel Materials

Professor Dimitri N. Basov

ABSTRACT OF THE DISSERTATION

Infrared probe of electrostatic doping in novel materials

by

Zhiqiang Li

Doctor of Philosophy in Physics
University of California, San Diego, 2008
Professor Dimitri N. Basov, Chair

In this thesis we investigate electrostatic doping of a wide variety of novel materials incorporated in field-effect transistors (FETs), including polymers, organic molecular crystals, graphene and bilayer graphene. These studies have lead to substantial advances in our current understanding of these materials. Specifically, we performed the first infrared (IR) imaging of the accumulation layer in poly(3-hexylthiophene) (P3HT) FETs. Furthermore, we found that charge carriers in molecular orbital bands with light mass dominate the transport properties of single crystal rubrene. More recently, we explored the IR absorption of graphene and found several signatures of many-body interactions. Moreover, we discovered an asymmetric band structure in bilayer graphene and determined the band parameters with an accuracy never achieved before. Our work has demonstrated that IR spectroscopy is uniquely suited for probing the electronic excitations in nanometer-thick accumulation layers in FET devices.

1

Introduction

In this thesis, infrared (IR) spectroscopy is employed to study the electrostatic doping of a wide variety of novel materials. Electrostatic modification of novel materials via field-effect transistors (FETs) is an emerging research area [1, 2]. Silicon FETs are ubiquitous in modern microelectronics, where the conductance of the semiconductor is modified by a gate voltage. Electrostatic modulation of the carrier density in novel materials can not only lead to changes in conductance but also induce fundamental modification of the electronic and magnetic properties of materials. This is because in many novel materials, such as transition metal oxides (high-Tc cuprates), magnetic semiconductors, low-dimensional systems (graphene), organic materials and many others, a change in the carrier density can lead to a rich spectrum of phase transitions [1, 2]. Electrostatic doping allows for controlled and reversible changes of the carrier concentration without modifying the level of disorder; therefore it is a very appealing method to study the intrinsic properties of materials. Furthermore, it is also promising for developing new devices with new functionalities.

IR spectroscopy is a unique technique to explore the physics of electrostatic doping. In FETs, the charge carriers are confined to a nanometer-thick layer at the semiconductor–insulator interface, buried under several layers of the device. This makes it extremely difficult to experimentally study the injected charge carriers using some of the most informative techniques in the arsenal of physicists and chemists,

including scanning tunneling microscopy, photoemission spectroscopy, and inelastic x-ray and neutron scattering. In contrast, IR spectroscopy can probe the electronic excitation in FETs in a broad energy range (~ 1meV-6eV) under strong electric field (~ 10^5V/cm) and high magnetic field (~ 31T). Employing IR radiation from a synchrotron, micro-size samples (~few microns) can be measured. Here, we report on IR studies of electrostatic doping in several novel systems. These investigations have lead to numerous significant advances in the fundamental understanding of these materials and their potential applications.

In chapter 2, a composite metal-polymer electrode is designed to investigate electric-field-induced changes of the dielectric function of gate insulators in metal-oxide-semiconductor structures using infrared spectroscopy. We studied structures based on TiO_2 dielectric insulator on doped silicon, a combination commonly used in field effect transistors. It is shown that the voltage-induced changes of the dielectric constant in TiO_2 originate from a modification of the lattice vibration modes of this compound [3].

In chapter 3, we report on IR spectro-microscopy of the electronic excitations in nanometer-thick accumulation layers in FET devices based on poly(3-hexylthiophene). IR data allows us to explore the charge injection landscape and uncovers the critical role of the gate insulator in defining relevant length scales. This work demonstrates the unique potential of IR spectroscopy for the investigation of physical phenomena at the nanoscale occurring at the semiconductor-insulator interface in FET devices [4].

In chapter 4, we present an infrared spectroscopy study of mobile holes in the accumulation layer of organic field-effect transistors based on rubrene single crystals.

Our data indicate that both transport and infrared properties of these transistors at room temperature are governed by light quasiparticles in molecular orbital bands with the effective masses m* comparable to free electron mass. Furthermore, the m* values inferred from our experiments are in agreement with those determined from band structure calculations. These findings reveal no evidence for prominent polaronic effects, which is at variance with the common beliefs of polaron formation in molecular solids [5].

In chapter 5, we performed an IR spectromicroscopy study of charge dynamics in graphene integrated in gated devices. Our measurements verify the expected characteristics of graphene and, owing to the previously unattainable accuracy of IR experiments, also uncover significant departures of the quasiparticle dynamics from predictions made for Dirac fermions in idealized, free standing graphene. Several observations reported here indicate the relevance of many body interactions to the electromagnetic response of graphene [6].

In chapter 6, we carried out infrared spectroscopy of bilayer graphene integrated in gated structures. We observed a significant asymmetry in the optical conductivity upon electrostatic doping of electrons and holes. We show that this finding arises from a marked asymmetry between the valence and conduction bands, which is mainly due to the inequivalence of the two sublattices within the graphene layer. From the conductivity data, the energy difference of the two sublattices and the interlayer coupling energy are directly determined [7].

In chapter 7, we studied charge dynamics in graphite in zero field and high magnetic fields. In 7.2, we present a systematic investigation of the ab plane and c-axis

optical conductivity of highly oriented pyrolytic graphite (HOPG) via infrared ellipsometry and reflectance measurements. Our data confirm that the optical conductivity of graphite per graphene layer is close to the universal conductivity of intrinsic graphene in the mid-infrared region. Moreover, these measurements have placed constraints on the c-axis optical conductivity of HOPG. In 7.3, we present a systematic investigation of the magneto-reflectance HOPG in magnetic field B up to 18T. From these measurements, we report the determination of lifetimes τ associated with the lowest Landau levels in the quantum limit. We find a linear field dependence for inverse lifetime $1/\tau(B)$ of the lowest Landau levels, which is consistent with the hypothesis of a three-dimensional (3D) to 1D crossover in an anisotropic 3D metal in the quantum limit. This enigmatic result uncovers the origin of the anomalous linear in-plane magneto-resistance observed both in bulk graphite and recently in mesoscopic graphite samples. [8].

2

An infrared probe of tunable dielectrics in metal-oxide-semiconductor structures

High dielectric constant ($\varepsilon_1(0)$) insulators have the potential to serve as alternative gate dielectric materials in metal-oxide-semiconductor (MOS) structures to circumvent the fundamental scaling limitations of SiO_2 [9]. Because enhanced values of $\varepsilon_1(0)$ in oxides stem from their giant ionic polarizabilities, these systems are inherently susceptible to applied electric fields [10, 11]. It is therefore prudent to characterize field-induced modifications of $\varepsilon_1(0)$ under operational conditions in realistic MOS devices. Conventional spectroscopic investigations of MOS structures usually utilize ultra-thin semi-transparent metallic electrodes [12, 13]. However, in these earlier works, experiments in the far-infrared (IR) were prohibitively difficult because of the poor transparency of the metallic electrodes [14]. Here we report on an electrode comprised of interdigitated Au contacts covered with a polymer film that is ideally suited for the study of electric field induced effects in the far-IR and applied this electrode to investigate field-induced changes of $\varepsilon_1(\omega\rightarrow 0)$ in TiO_2 incorporated in a MOS structure. We show that the origin of voltage-induced changes of $\varepsilon_1(0)$ is the hardening of IR-active phonons in TiO_2.

An example of the MOS structure explored in this work is displayed in the left panel of Fig. 2.1. In these structures a 180 nm layer of TiO_2 is deposited on a 500 μm

n-doped Si substrate which also serves as the gate electrode. A 6 nm SiO_2 layer is deposited onto the TiO_2 layer [15]. The SiO_2/TiO_2 bilayer significantly improves the characteristics of P3HT based FET device compared to a single layer of TiO_2. Interdigitated source and drain gold contacts form a grid on the insulating layer with the grid spacing ranging from 50 μm to 200 μm. Contacts for standard four-probe measurements are also deposited enabling monitoring of the I-V characteristics of the particular device employed for the spectroscopic study. The final stage of the device fabrication is coating with a 4 nm thin film of poly(3-hexylthiophene) (P3HT). Charge injection into the accumulation layer in the polymer film[16] allows one to maintain an electric field in the region between the thick Au grids, a virtue not offered by ordinary interdigitated electrodes. Because the polymer film is highly transparent even under charge injection, these large area (>1 cm^2) "grid-electrode" structures offer significant advantages over conventional approaches [12-14] to study the modifications of optical properties by applied electric field. Here we will focus on the analysis of voltage-induced modifications of TiO_2 in the far-IR region facilitated by grid-electrode structures; spectroscopic studies of the effects of applied electric field on the polymer will be reported separately.

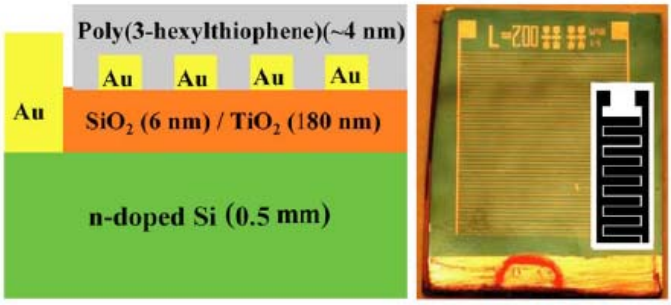

Figure 2.1: Left panel: a schematic of the MOS device with a composite metal-polymer top electrode. Right panel: a photograph of the actual device along with a schematic representation of the electrodes. The Au bar at the bottom of the structure is a contact to the substrate. The contacts on the top of the structure are intended for four-probe measurements of I-V characteristics.

In Fig. 2.2 we summarize our results for a representative composite electrode device. The top panel shows the ratios of transmission spectra at different voltages applied between the Si substrate and Au grid-electrodes normalized by transmission at V=0: $T(\omega,V)/T(\omega,0)$. All spectra were measured at room temperature with unpolarized light, with a spectral resolution of 1 cm^{-1}. The middle panel displays the absolute transmission of the device at zero applied voltage and at V=45 V. The dips in the $T(\omega)$ spectra of the device at 216, 386 and 503 cm^{-1} are due to absorptions associated with the transverse optical (TO) phonon modes of TiO_2 [17, 18]. When a biasing voltage is applied to the device these modes harden (middle panel of Fig. 2.2) leading to strong resonances in the $T(\omega,V)/T(\omega,0)$ spectra. Transmission changes reach 10% near 200 cm^{-1} at 45 V, a voltage close to the breakdown threshold of these devices. A reference structure without a polymer film did not show appreciable changes in $T(\omega)$ suggesting that the effect is intimately related to the presence of the electric field between the Au contacts. Indeed, under the applied voltage the SiO_2/TiO_2 bilayer is

effectively placed in a capacitor formed by charge-injected polymer at the top and n-Si substrate at the bottom. Note that the Au grid electrodes are not transparent in the far-IR region. Therefore, the field-induced changes of optical properties of the sample are produced primarily by the polymer and SiO_2/TiO_2 in regions between the Au bars.

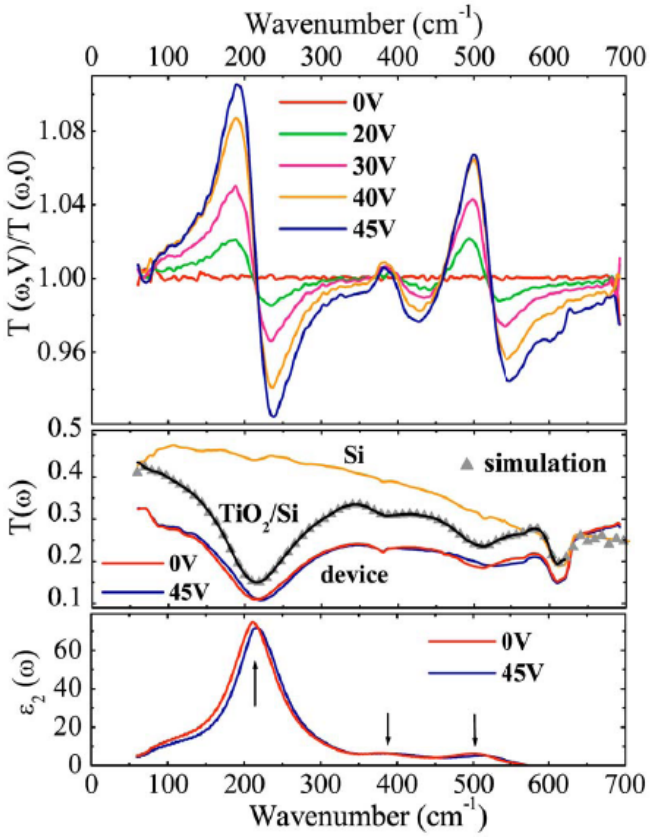

Figure 2.2: Top panel: the ratios of transmission spectra of a device with a grid spacing of 50 μm at different applied voltages between the Si substrate and Au grid-electrodes. The same potential was applied to the source and drain, therefore the source-drain current was zero. Middle panel: the transmission spectrum of the Si substrate and the TiO_2/Si bilayer. With the carrier concentration in the n-Si in the 10^{18} cm^{-3} range, the substrate and therefore the entire device shows relatively high transmission T(ω)≈20-50% in the far-IR region. A fit of T(ω) for the TiO_2/Si bilayer using a Kramers-Kronig (KK) constrained algorithm is represented by gray triangles. T(ω) of the device at 0V (red line) and 45V (blue line). Bottom panel: $\varepsilon_2(\omega)$ of the TiO_2 film at zero applied voltage and 45V extracted from the KK constrained fitting. The three absorptions peaks (marked by arrows) in $\varepsilon_2(\omega)$ are due to the TO modes of the TiO_2 film. Under applied field the TO frequencies harden as evident from both transmission data and $\varepsilon_2(\omega)$ spectra.

In order to quantify the field-induced modifications of the IR response of TiO_2 it is imperative to evaluate the optical constants of all layers constituting our P3HT/SiO_2/TiO_2/n-Si devices. The complex dielectric function of the n-Si substrate

$\varepsilon^{Si}(\omega)$ was determined from a combination of transmission T(ω) and reflectance R(ω) measurements [19]. Next, we measured T(ω) spectra for a TiO_2/n-Si bilayer. The complex dielectric function of TiO_2 $\hat{\varepsilon}^{TiO_2}(\omega) = \varepsilon_1^{TiO_2}(\omega) + i\varepsilon_2^{TiO_2}(\omega)$ was then evaluated from these measurements using a Kramers-Kronig constrained fitting algorithm [20] by properly including multiple reflections occurring in the TiO_2/n-Si bilayer. Within the absolute uncertainty of our measurements (0.5%) the 6nm layer of SiO_2 did not produce a noticeable effect on the T(ω) of the device and was ignored in the analysis. We have verified that the absorption associated with the accumulation layer in P3HT and in n-Si has no impact on the T(ω) spectra in the frequency region of TiO_2 phonons. Therefore, it is unnecessary to account for the response of accumulation layers in the analysis. As expected, the primary effect of the gold grid is to reduce the absolute value of the T(ω) of the device without introducing new features to T(ω) in the concerned frequency range where the phonon modes of TiO_2 dominate the IR response (middle panel of Fig. 2.2).

The dielectric function of the TiO_2 layer (Fig. 2.2 and Fig. 2.3) extracted from the analysis detailed above displays 3 resonances that can be described with the usual Lorentzian form:

$$\varepsilon(\omega) = \varepsilon_\infty + \sum_j \frac{\omega_{Pj}^2}{\omega_{0j}^2 - \omega^2 - i\gamma_j\omega} \qquad (2.1)$$

where γ_j and ω_{pj} are the linewidth and plasma frequency of the j-th mode at ω_{0j} respectively. Field-induced hardening of TO modes of TiO_2 evident in the raw T(ω) data for our devices is also clearly seen in the spectra of the real and imaginary part of

the dielectric function of the TiO_2 layer. All three TO modes harden by approximately 3% at 45V (Fig. 2.3). Frequencies for the longitudinal optical (LO) modes of TiO_2 can be obtained from Eq. 2.1 using the relationship $\omega_{LOj}^2 = \omega_{TOj}^2 + \omega_{pj}^2$. The TO and LO phonon modes for both the TiO_2 film and bulk TiO_2 with rutile structure[9] are listed in Table 2.1. The modification of the lattice dynamics of TiO_2 by applied electric field is not unexpected since TiO_2 is an incipient ferroelectric [21]. Indeed, field-induced changes of the static dielectric constant $\varepsilon_1(0)$ have been previously reported for other ferroelectrics [22, 23]. The real part of the dielectric function $\varepsilon_1(\omega)$ of TiO_2 gate insulator is plotted in the bottom panel of Fig 2.3. The bottom inset of Fig 2.3 also displays the voltage dependence of $\varepsilon_1(\omega = 60\ cm^{-1})$ along with the zero frequency extrapolation of $\varepsilon_1(\omega)$, which is a reliable estimate of $\varepsilon_1(0)$. The $\varepsilon_1(0)$ of TiO_2 film obtained from our infrared measurements (~ 42) is consistent with capacitive measurements (~ 41).[7] However, both of these results are significantly smaller than the bulk value reported for crystalline TiO_2 (~90) [21].

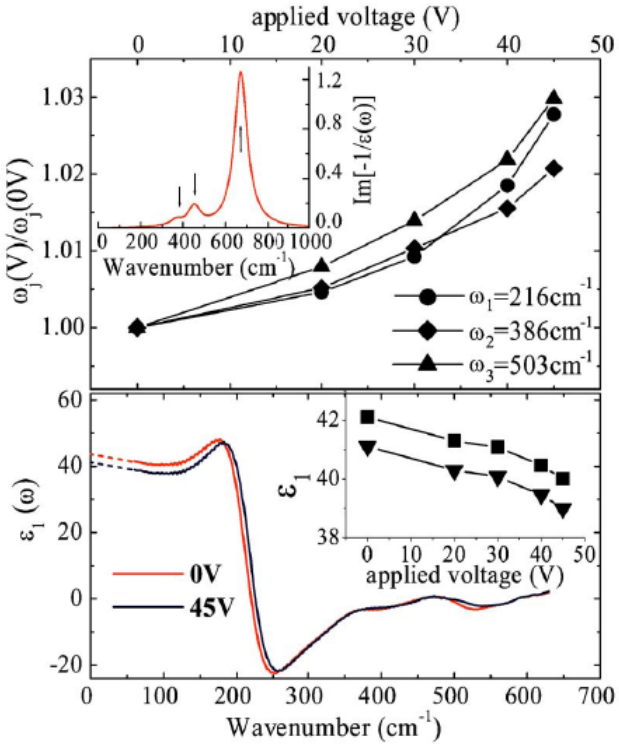

Figure 2.3: The loss function Im[-1/ε(ω)] (top inset) and the real part of the dielectric function $\varepsilon_1(\omega)$ (bottom panel) of the TiO_2 film obtained from the KK constrained fitting of the transmission spectra. The peaks marked by arrows in top inset are the LO modes of the TiO_2 film. The dashed lines below 60 cm^{-1} are extrapolations of $\varepsilon_1(\omega)$ to zero frequency. Top panel: the ratios of TO phonon frequencies of the TiO_2 film with and without applied voltage from Table 2.1. Bottom inset: ε_1 at 60cm^{-1} (solid triangle) and zero frequency extrapolation $\varepsilon_1(\omega\rightarrow 0)$ (solid square) of the TiO_2 film at different applied voltages. Under applied voltage the phonon resonances harden whereas the absolute value of the static dielectric constant is reduced.

Insights into the reduction of $\varepsilon_1(0)$ in films compared to that of bulk crystals and into its field-induced modification are provided by the Lyddane-Sachs-Teller (LST) relation [24]:

$$\frac{\varepsilon_1(0)}{\varepsilon_\infty} = \prod_{j=1}^{N} \frac{\omega_{LOj}^2}{\omega_{TOj}^2} \qquad (2.2)$$

The relation connects $\varepsilon_1(0)$ and the high frequency dielectric constant ε_∞ to the frequencies of LO and TO phonon modes of a crystal (ω_{LOj} and ω_{TOj} respectively). Using the values in table 2.1 together with ε_∞~6.84 for rutile [25] and ε_∞~5 for the TiO_2 thin film from our modeling, we obtain $\varepsilon_1(0)$~103 for the crystal and $\varepsilon_1(0)$~37 for the TiO_2 film from eq. (2.2). Therefore the reduction of $\varepsilon_1(0)$ in the film is a consequence of smaller TO-LO splitting compared to that of a bulk material. The field-induced changes of $\varepsilon_1(0)$ are also consistent with the LST relation. Indeed, the voltage induced hardening of the TO modes fully accounts for the reduction of $\varepsilon_1(0)$ by about 3% (as shown in bottom inset of Fig 2.3). Our measurements demonstrate that *all* TO modes of the TiO_2 film are modified by applied electric field. This finding is in accord with Cochran's theory of ferroelectricity [10], where all non-linear terms in the short range forces are equally important. An interconnection between the field-induced modification of phonon frequencies and the reduction of $\varepsilon_1(0)$ reported here affords adjustable dielectric characteristics widely employed in tunable microwave devices [11].

In conclusion, we show that a composite metal-polymer electrode enables far-IR spectroscopic characterization of gate insulators exploited in the MOS architecture. Our results reveal that the microscopic origins of tunable dielectric response of the TiO_2 gate insulator are associated with the hardening of TO phonons in applied electric fields. The characterization capabilities documented here uncover the unique potential of infrared spectroscopy for the analysis of tunable insulators and also for examination of charge injection phenomena in semiconductors.

Table 2.1: the TO and LO frequencies of the j-th phonon mode (ω_{TOj} and ω_{LOj}, in cm^{-1}) of the TiO_2 film at 0V and 45V and those of bulk TiO_2 with rutile structure. The uncertainty of the TO frequencies is 1 cm^{-1} (our spectral resolution) and that of the LO frequencies is less than 10 cm^{-1} (the uncertainty of our simulation.).

	ω_{TO1}	ω_{TO2}	ω_{TO3}	ω_{LO1}	ω_{LO2}	ω_{LO3}
TiO_2 film	216	386	503	672	376	453
TiO_2 film (45V)	222	394	518	680	379	466
Bulk TiO_2 (rutile)[a]	183	388	500	807	373	458

[a] Ref. [17].

Acknowledgements: This chapter contains materials in Z.Q. Li, G.M. Wang, K.J. Mikolaitis, D.Moses, A. J. Heeger, and D.N. Basov, "*An infrared probe of tunable dielectrics in metal-oxide-semiconductor structures*", Appl. Phys. Lett. 86, 223506 (2005). The dissertation author was the primary investigator and author of this paper. The coauthors of this paper all contribute to the studies describe in this chapter.

3

Infrared imaging of the nanometer-thick accumulation layer in organic field-effect transistors

The field-effect transistor (FET) is a benchmark system for exploring the properties of a broad variety of materials as well as for exploiting their novel functionalities. Fundamentally, the electrostatic modulation of carrier density using the FET principle occurs at nanometer scales since the enhanced density of injected charges extends over only few nanometers within the active material [26]. The bottom contact FET devices (schematics in Fig. 3.1) are particularly well suited for the studies of electrostatic doping of macroscopic samples of novel low-dimensional nanoscale systems[27] such as films of polymer chains[28], nanotubes[29], molecules[30] and possibly even DNA bundles[31], all of which can be easily deposited atop of patterned electrodes. So far, experimental studies of the above FET structures have been primarily limited to transport measurements. New insights into the dynamical properties of the injected carriers are expected from spectroscopic characterization of the electronic excitations in the accumulation layer. However, this is a challenging task given the fact that these layers are exceptionally thin, in the nanometer range. In this letter, we demonstrate the capability of infrared (IR) spectroscopy to explore the electronic

excitations in nanometer-thick accumulation layers in bottom-contact FET devices focusing on charge injection in poly(3-hexylthiophene) (P3HT) thin films. We have developed a platform that enables both IR spectroscopic and transport investigations of charge injection in the same device: an essential experimental step towards consistent analysis of transport and spectroscopic data. Earlier IR measurements on charge injection in organic thin films have been reported only in metal-insulator-semiconductor structures, which are distinct from bottom-contact FET devices typically employed for transport studies[13, 14, 32].

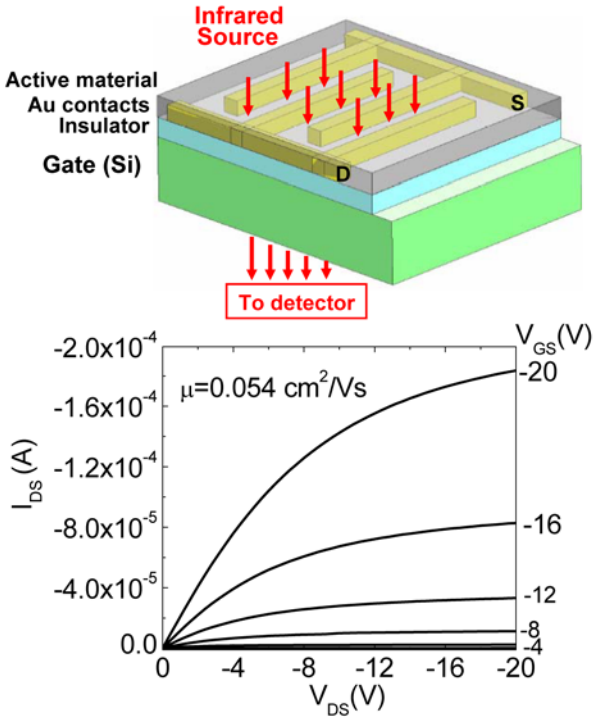

Figure 3.1: Top panel: schematic of a FET device in the bottom-contact geometry for infrared characterization of charge injection. The active material in our FET devices is P3HT. Bottom panel: the I-V curve of a representative TiO_2-based FET.

We studied bottom-contact organic FET devices (Fig. 3.1) based on P3HT, a semiconducting polymer with exceptionally high mobility[33]. Devices employing a high dielectric constant (κ) insulator TiO_2 [15] as well as SiO_2 [34] were investigated. The goal of using high-κ insulator is to increase the injected carrier density compared to SiO_2-based devices [15]. For either type of transistors we have succeeded in probing the electronic excitations in the nanometer thick accumulation layer under applied fields exceeding 10^7 V/cm: *a regime that has never been explored previously in spectroscopic studies*. An analysis of the oscillator strength of the spectroscopic signatures of charge injection allowed us to quantify the density of the injected carriers and examine its evolution with applied voltages. Using IR microscopy we were able to monitor the spatial dependence of the injected charges in the active area of the device. Our results for the high-κ devices show significant departures from the behavior expected for an "ideal" FET [35] in which the charge density increases linearly with voltages and is uniform in the channel. This study uncovers the unique potential of IR spectroscopy for investigating the dynamical properties of the electronic excitations in FET structures.

Large area FET devices (>1 cm^2) with gate insulator deposited on n-Si were investigated in this work [3]. We employed two types of gate insulators: 200 nm thick SiO_2 and SiO_2(6 nm)/TiO_2(180 nm) bilayer; we will refer to the latter devices as "TiO_2-based". The transport mobility of P3HT in our SiO_2-based transistors [34] is 0.18 $cm^2V^{-1}s^{-1}$, whereas that in TiO_2-based FETs [15] is 0.05 $cm^2V^{-1}s^{-1}$. The I-V curve for a typical TiO_2-based FET is shown in the bottom panel of Fig. 3.1. In this paper we focus on the results for TiO_2-based devices. In these FET devices, source and drain Au electrodes

(with a spacing of 50-200 μm) were patterned on insulating oxides followed by the deposition of a 4 – 6 nm-thick P3HT film. Fig. 3.1 shows a cross-section of the devices whereas Fig. 3.4d depicts a top view photograph of an actual device. The breakdown voltage of TiO_2-based devices is about -35~ -45 V and that of SiO_2 -based FETs exceeds -100V. In bottom-contact FET devices, an applied gate voltage induces an accumulation layer [28, 36] in P3HT that forms the p-type conducting channel between the Au electrodes. This channel is not obscured by any other interfaces from above and is therefore well suited for the spectroscopic studies [3] of the accumulation layer in the polymer film from far-IR to near-IR with the latter cut-off imposed by the band gap of Si substrate. To examine the length scales associated with charge injection we fabricated devices with a "V-shape" electrode pattern (Fig, 3.4b). We studied changes of transmission as a function of applied gate voltage V_{GS} normalized by the transmission at V_{GS}=0: $T(\omega,V_{GS})/T(\omega,V_{GS}=0)$. The source and drain electrodes were held at the same potential in most measurements. All the data reported here were recorded at room temperature with a spectral resolution of 4 cm^{-1}.

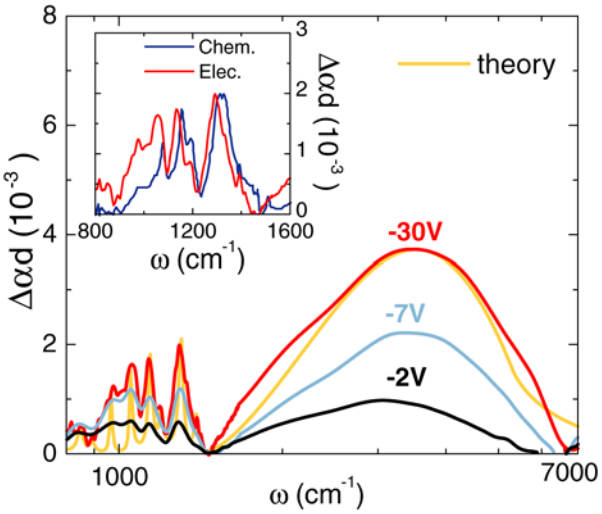

Figure 3.2: The voltage-induced absorption spectra Δαd for the P3HT layer under applied gate voltages V_{GS} in a TiO_2-based device. The green curve is a theoretical modeling of the experimental spectrum as detailed in Supporting Information. **Inset:** Δαd spectrum for a representative TiO_2 based device at V_{GS}=-30V along with the data for chemically doped P3HT[37]. The latter is the difference spectrum between the absorption of chemically doped P3HT with 1 mol % PF_6^- and that of pure P3HT[37] scaled by a factor of $4*10^5$. All spectra uncover spectroscopic fingerprints of electrostatic doping: IRAV modes in 1,000-1,500 cm^{-1} range and a polaron band at 3,500 cm^{-1}. The oscillator strength of both the polaron band and the IRAV modes increases with gate voltage. The noise of the Δαd spectra is less than 10^{-4}.

The absorption spectra $\Delta\alpha d = 1-T(V_{GS})/T(0V)$ of TiO_2-based devices are displayed in Fig. 3.2. Here Δα is the change of the absorption coefficient of P3HT with applied voltage and d is the thickness of the accumulation layer. These spectra show two voltage-induced features: i) sharp resonances in the 1,000 -- 1,500 cm^{-1} region, and ii) a broad band centered around 3,500 cm^{-1}. A gradual development of these features with increasing gate voltage V_{GS} suggests that they are intimately related to the formation of charge accumulation layer in P3HT. (Due to the imperfections of the TiO_2/Si boundary as well as of the surface phonon scattering [38] originating from the

large polarizability of high-κ insulator TiO_2, absorption associated with the accumulation layer in n-Si is spread out over a broad frequency range and has a negligible contribution to the absorption spectra in the far-IR[3] and mid-IR. Therefore, the $\Delta\alpha d$ spectra displayed in Fig. 3.2 can be attributed to the voltage-induced carriers in P3HT.) This assignment is supported by earlier reports of similar changes of optical properties produced by photoexcitation [37, 39, 40], chemical doping [37, 39] or electrostatic charge doping achieved by placing a P3HT film between semi-transparent electrodes[13, 14, 32]. Sharp resonances in the 1,000-1,500 cm^{-1} range result from the IR active vibrational modes (IRAVs); i.e Raman modes made IR active by distortions of the polymer backbone caused by the self-localized charges[39]. The frequencies of the IRAV modes are in excellent agreement with the vibrational resonances found in chemically doped P3HT (inset of Fig. 3.2). The broad absorption band centered around 3,500 cm^{-1} is usually ascribed to a midgap state of polaron or bipolaron associated with the local relaxation of the lattice around the doped charge[39]. Whether this absorption is due to polaron or bipolaron is still under investigation [13, 37]. We'll refer to this broad absorption band as polaron for simplicity. Both the IRAV modes and the polaron band can be quantitatively described by the amplitude mode model [41, 42] of charge excitations in conjugated polymers. A theoretical fit of the experimental results based on this model is shown in Fig. 3.2 (see Supporting Information for details). Similar features due to IRAV modes and polaron are also observed in SiO_2-based devices as will be discussed in details in an upcoming publication.

With the key spectroscopic signatures of charge injection in P3HT established for our open channel devices (Fig. 3.2) we now turn to the analysis of their oscillator strength. It is instructive to define the effective spectral weight as $N_{eff} = \int (\Delta \alpha d) d\omega$, which is proportional to the 2D density of the injected charges responsible for the absorption structure in our data. Notably, the polaron band and IRAV modes are well separated from each other in the spectra in Fig. 3.2 and therefore the oscillator strength of these two structures can be quantified by properly choosing the integration cut-offs. Fig. 3.3 displays the spectral weight of the polaron band N_{eff}^{P} (integrated from 1,450 cm^{-1} to 6,000 cm^{-1}) and that of the highest energy IRAV mode N_{eff}^{IRAV} (integrated from 1,200 cm^{-1} to 1,450 cm^{-1}) plotted as a function of V_{GS}. A gradual growth of both N_{eff}^{P} and N_{eff}^{IRAV} with the increase of V_{GS} is observed. The simple capacitive model of an FET device predicts the linear dependence between the charge density and the bias voltage with the slope determined solely by the dielectric constant of the gate insulator κ and the thickness of the insulator L:

$$N_{2D} = \frac{\kappa \varepsilon_0}{eL} V_{GS} . \qquad (3.1)$$

Devices based on TiO_2 reveal a linear voltage dependence of $N_{eff}(V_{GS})$ at small V_{GS} with an obvious trend to saturation at higher biases.

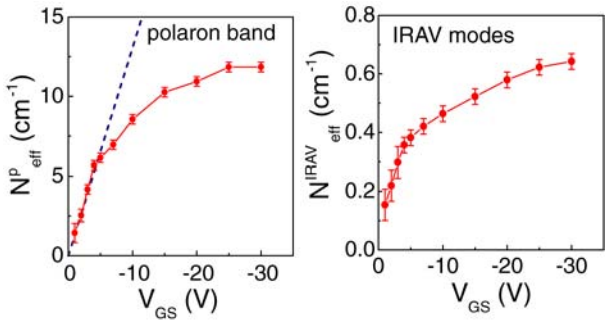

Figure 3.3: Evolution of the spectral weight of the polaron band $N_{eff}^{P}(V_{GS})$ (left panel) and of the IRAV modes $N_{eff}^{IRAV}(V_{GS})$ (right panel) with gate voltage V_{GS} in a TiO_2-based device. The dashed line in the left panel represents the linear V_{GS}-dependence of $\boldsymbol{N_{eff}^{P}}$ from a capacitive model.

Below we show that valuable insights into the accumulation layer characteristics are provided by a survey of the spatial distribution of charge density in the FET devices using IR microscopy. We carried out microscopic study of the excitations associated with the electrostatically doped charges in P3HT using the infrared beamlines at the Advanced Light Source (ALS) facility. With the focused beam of an IR microscope we were able to record spectra similar to those displayed in Fig. 3.2 from areas as small as 50-100 μm in diameter. The IR beam was scanned in between the "V" shaped electrodes (Fig. 3.4b) or in the corner of the electrodes in Fig. 3.4d with simultaneous monitoring of the voltage-induced changes in the spectra. The frequency dependence of absorption spectra did not change appreciably throughout the entire device. We therefore focus on the spatial dependence of the integrated weight of both IRAVs and of the polaron band. In Fig. 3.4a we plot the spectral weight of the highest frequency IRAV mode of P3HT as a function of separation between the V-shaped electrodes l normalized by data at l=0: $N_{eff}^{IRAV}(l)/N_{eff}^{IRAV}(l=0)$. TiO_2-based FETs reveal a gradual

decay of the injected charge density away from the electrodes that vanishes at length scales of about 500 μm. The decay of the injected carrier density in FETs with TiO_2 gate insulator is also evident in the 2D charge density profile $N_{eff}^{IRAV}(x,y)$ shown in Fig. 3.4c. Here $N_{eff}^{IRAV}(x,y)$ vanishes at distances beyond 500-600 μm away from the electrodes in accord with the data for V-shaped structures. On the contrary, FETs structures with SiO_2 gate insulator show no change of carrier density at least up to 1.6 mm away from the contacts. This latter result verifies that in SiO_2-based FETs a uniform equipotential layer is formed consistent with the notion of an "ideal" field effect transistor [35]. The charge injection landscape was also explored by imaging the polaron absorption with a spatial resolution of 3 μm in a set-up based on synchrotron source at the ALS. These fine resolution results are identical to those inferred from IRAV modes: a gradual decrease of N_{eff}^{P} in TiO_2-based devices and no measurable decrease of N_{eff}^{P} in SiO_2-based structures. Neither result significantly depends on the biasing voltage. To the best of our knowledge, this is the first spatially-resolved IR imaging of the injected charges in FETs.

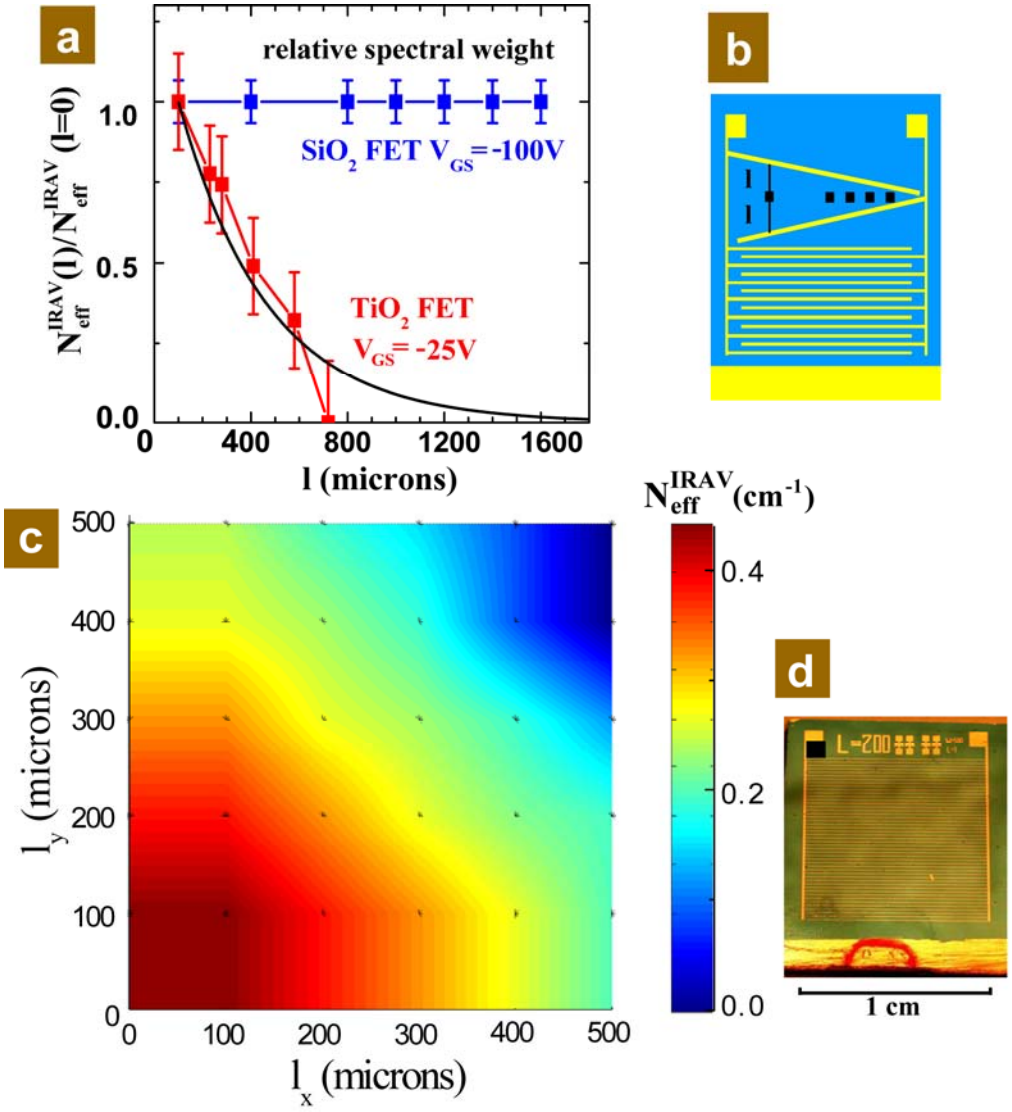

Figure 3.4: Infrared imaging of the charge injection landscape in several representative FETs. **a**, the spectral weight of IRAV modes of P3HT as a function of separation between the V-shaped electrodes *l* normalized by data at *l*=0: $N_{eff}^{IRAV}(l)/N_{eff}^{IRAV}(l=0)$, indicated by the black squares in **b** for devices with "V" shape electrodes**.** The black curve in **a** shows a fit of N(l)/N(l=0) with an exponential form.[24] **c,** the 2D charge profile $N_{eff}^{IRAV}(l_x,l_y)$ in the P3HT layer of an FET with TiO_2 gate insulator under -25V. The mapping region is the up-left corner of the electrode as schematically shown in **d** by the black square. The charge injection landscape inferred from the polaron absorption is identical to **a** and **c** generated via monitoring of the IRAV modes. The length scale of the charge injection process in FETs with TiO_2 gate insulator is several hundred microns, whereas the injected charges form a uniform layer in FETs with SiO_2 gate insulator and the charge injection length scale is 1.6mm or even longer.

The saturation behavior (Fig. 3.3) of the spectral weight of *localized excitations*, i.e., $N_{eff}^{P}(V_{GS})$ and $N_{eff}^{IRAV}(V_{GS})$, may be indicative of the precursor to the insulator-to-metal transition in conjugated polymers [43] at high carrier density. However, this intriguing interpretation has to be critically examined since several other factors can in principle mimic the saturated or nonlinear voltage dependence of the localized modes, such as the high leakage currents exceeding hundred μA at high voltages observed in TiO_2-based FETs. A gradual decay of charge density in the accumulation layer in TiO_2-based FETs revealed by IR imaging experiments probably originates from the imperfections of the gate dielectric/polymer interface as well as high leakage currents. Naturally, charges that are either trapped at the insulator/polymer interface or leak through the insulator do not contribute to the oscillator strength of the features in the absorption spectra. Therefore injected charges are registered in our imaging studies only after they exhaust all potential leakage paths through the insulator and traps at the polymer/insulator interface. The length scale limiting propagation of charges away from the injection contacts naturally follows as a result of competition between the channel resistance and the leakage resistance of the gate insulator[44]. These IR microscopy results indicate that the saturation of the oscillator strength of localized excitations at high V_{GS} biases is extrinsic and originates from the limitations of TiO_2 gate insulator.

In a recent work [45], we carried out a comprehensive theoretical and experimental study of charge injection in P3HT to determine the most likely scenario for metal-insulator transition in this system. We analyzed the electronic excitations for three possible scenarios under which a first- or a second-order metal-insulator transition can occur in doped P3HT. Our measurements and theoretical predictions suggest that

charge-induced localized states in P3HT FETs are bipolarons and that the highest doping level achieved in our experiments approaches that required for a first-order metal-insulator transition.

In summary, IR spectroscopy investigations of the electronic excitations in a nanometer thick accumulation layer, i.e., IRAV modes and polarons, have been carried out in P3HT thin film FET devices. We show that the unconventional behavior in TiO_2-based FETs is due to the limitations of the TiO_2 gate insulator. Our work has demonstrated that IR spectroscopy is a unique technique for the study of charge injection in macroscopic samples of nanometer-scale materials in bottom-contact FET devices. Instrumental innovations reported here uncover the potential of IR spectro-microscopy for the investigation of both IRAV modes and polarons, which are of fundamental importance for the understanding of charge transport in other materials as well, such as DNA [46, 47].

3.A Supporting Information

Theoretical description of the field-induced absorption spectrum of P3HT.

We have fitted the field-induced absorption spectrum of P3HT using the amplitude mode model [41, 42] of charge excitations in conjugated polymers. In the generalized theory [42] for systems that do not satisfy the adiabatic approximation, i.e., all phonon frequencies are much smaller than the electronic band gap, the frequency dependent electrical conductivity is given by

$$\sigma(\omega) = \frac{\omega_P^2}{4\pi i\omega}\left\{ f(\omega)\frac{1 + D_0(\omega)[1-\alpha]}{1 + D_0(\omega)[1 + c(\omega) - \alpha]} - 1 \right\},$$

where $D_0(\omega) = \sum \frac{\lambda_n}{\lambda} \frac{\omega_{n0}^2}{\omega^2 - \omega_{n0}^2}$ is the phonon response function for the vibrational modes, ω_{n0} and λ_n are, respectively, the bare phonon frequencies and electron-phonon coupling parameter for the *n*th mode. Other parameters in this model are $f(\omega) = \frac{E_r^2}{\omega^2 y} \arctan(1/y)$ when $\omega < E_r$, and $f(\omega) = \frac{E_r^2}{2\omega^2 y}[\ln\frac{1-y}{1+y} + i\pi]$ when $\omega > E_r$, where $y = \sqrt{|1 - E_r^2/\omega^2|}$, E_r is the polaron relaxation energy, $c(\omega) = \frac{\lambda\omega^2 f(\omega)}{E_r^2}$, α is the pinning parameter associated with the field-induced polarons and $\lambda = \sum \lambda_n$ is the dimensionless coupling constant. Nine bare phonon frequencies are used to fit the experimental spectrum in Fig. 3.2, all of which are in good agreement with the phonon frequencies extracted from experiment in Ref. 20. The fitting parameters used for the theoretical spectrum in Fig. 3.2 are E_r=3,380 cm^{-1}, λ=0.2 and α=0.09. The good agreement between the experimental spectrum and that from theoretical modeling corroborates the microscopic origins of the observed field-induced absorption spectrum in Fig. 3.2.

Acknowledgements: This chapter contains materials in Z.Q. Li, G.M. Wang, N. Sai, D. Moses, M.C. Martin, M. Di Ventra, A.J. Heeger, and D.N. Basov, "*Infrared Imaging of the Nanometer-Thick Accumulation Layer in Organic Field-Effect Transistors*", Nano Letters 6, 224 (2006). The dissertation author was the primary investigator and author of this paper. The coauthors of this paper all contribute to the studies describe in this chapter.

4

Light quasiparticles dominate electronic transport in molecular crystal field-effect transistors

A comprehensive understanding of charge transport in organic semiconductors poses a significant intellectual challenge and, at the same time, is crucial for further advances in the field of “plastic electronics”[28, 48, 49]. One longstanding problem pertains to the nature of electronic excitations responsible for charge transport in these systems [50-52]. A commonly used description [50, 51] is that the electrical current in these easily polarizable materials is carried by polarons: electrons or holes strongly coupled to local lattice deformations, as illustrated in Fig. 4.0. A hallmark of the polaronic transport is a strong enhancement of the effective mass m* compared to the band values due to the coupling to the lattice [50, 51], which can be 10-1000 times heavier than the band mass. Therefore, the hypothesis of polaron formation in molecular crystals is verifiable since the effective masses of mobile charges can be directly probed in infrared (IR) spectroscopic measurements.

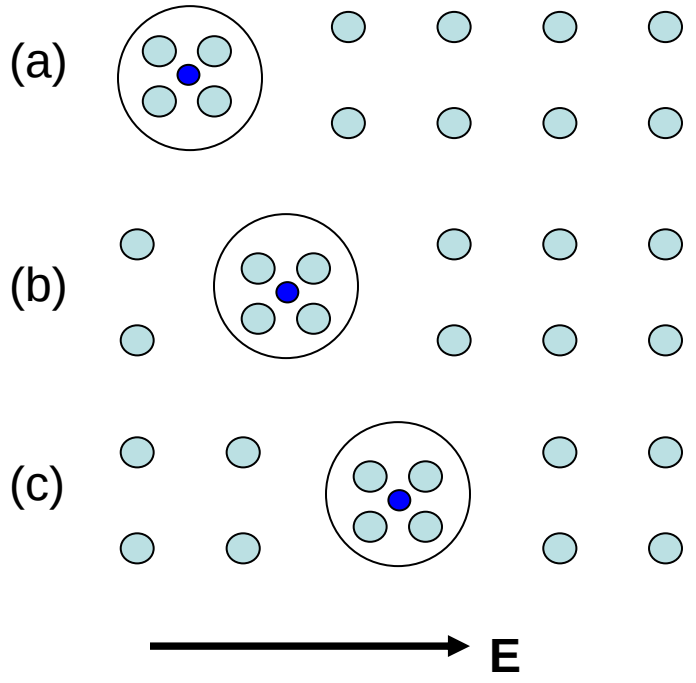

Figure 4.0: Panel (a)-(c) illustrate the formation of a small polaron (indicated by the large circle) and its motion in an electric field **E**. The small blue dot represents a charge carrier. The large solid dots are molecules. Because the van der Waals interactions between molecules are weak, molecular crystals are easily polarizable. When a charge carrier is injected into the material, local lattice distortions will be induced around the charge due to electrostatic interactions. Under an applied electric field **E**, the charge carriers will drag the local lattice distortions with them, forming the so-called small polarons. As shown here, small polarons usually have very heavy masses.

Here we report on IR spectroscopy studies of charge carriers in the conducting channel of organic field-effect transistors (OFET) based on single crystals of rubrene ($C_{42}H_{28}$, Fig. 4.1b inset), a small-molecule organic semiconductor [52-55]. Rubrene shows the highest mobility in organic materials, up to 20 cm^2/Vs at 300K. Previous transport studies revealed signatures of band-like transport in rubrene, such as an anisotropic electronic mobility, an increase of mobility at low temperature and the

observation of Hall effect [52-55]. These properties make rubrene a unique system for the study of the intrinsic charge transport in organic molecular crystals.

Our IR studies show that charge transport in rubrene based OFETs at room temperature is dominated by light quasiparticles in the highest occupied molecular orbital(HOMO) band. New spectroscopy data along with band structure calculations help to elucidate recent observations of non-activated, diffusive charge transport at the surface of high-quality molecular crystals in studies of single-crystal OFETs [52-55].

A schematic of the rubrene OFETs studied here is displayed in the inset of Fig. 4.1a. In these devices, source and drain graphite or silver paint contacts were prepared on the surface of a rubrene single crystal followed by the deposition of approximately 1 μm of parylene which serves as the gate insulator [53]. The gate-channel capacitance per unit area C_t in this type of devices is ~2.1 nF/cm^2. As a gate electrode, we used a 24-nm-thick layer of $InSnO_x$ (ITO) with the electron density $5*10^{20}$ cm^{-3} and the sheet resistance 300 Ω/square, deposited by a dc-magnetron sputtering in pure argon. The gate electrode covers the entire device area (up to 3x3 mm^2). We investigated the IR response of numerous transistors with typical DC transport mobility $\mu \cong 5$ cm^{2}V^{-1}s^{-1} at room temperature. The use of the semitransparent electrode ITO enabled spectroscopic studies of the field-induced accumulation layer (AL) in rubrene from far-IR up to 2.2 eV, the band gap of rubrene. In our IR measurements, free-standing rubrene OFETs were illuminated with linearly polarized light over the frequency range 30 - 18000 cm^{-1} (4 meV-2.2 eV) with a spectral resolution of 4 cm^{-1} using a home-built set-up for broad band micro-spectroscopy. We investigated the IR transmission of the OFETs,

$T(\omega, V_{GS})$, as a function of the frequency ω and the voltage applied between the source and gate electrodes, V_{GS} [56]. The source and drain electrodes were held at the same potential in most measurements.

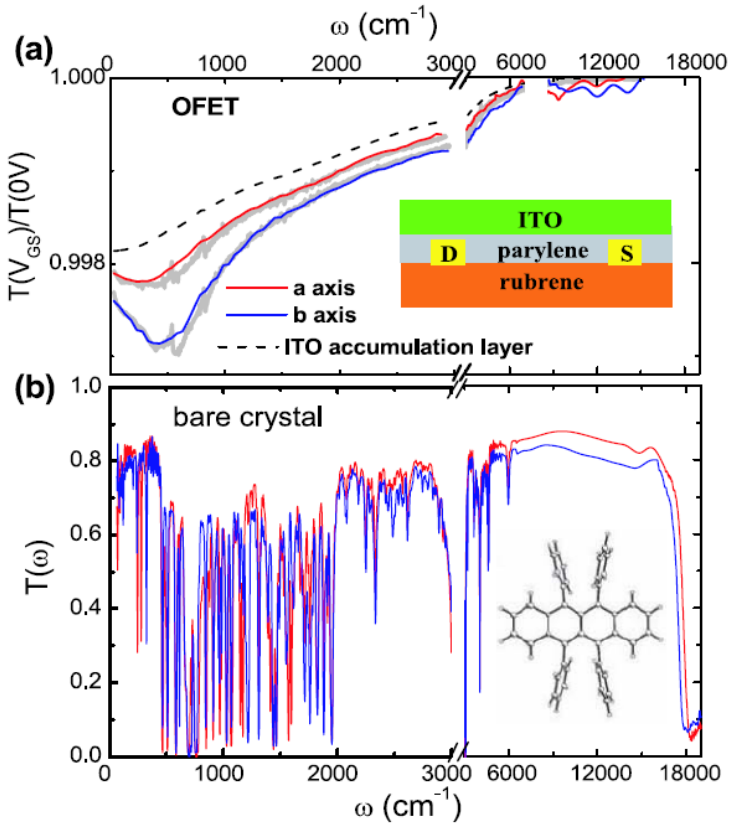

Figure 4.1: (a): voltage-induced changes of the transmission spectra $T(\omega,V_{GS})/T(\omega,V_{GS}=0V)$ for a representative rubrene OFET device at V_{GS}=-280V at room temperature. Thick gray lines: model spectra at -280V obtained from a multilayer analysis as described in the text. Dash line: the contribution of ITO accumulation layer to $T(\omega,V_{GS})/T(\omega,V_{GS}=0V)$ spectra. Inset of (a): a schematic of the OFET devices. (b): $T(\omega)$ of a bare rubrene crystal. Inset of (b): the molecular structure of rubrene.

We start by examining the transmission spectrum $T(\omega)$ of a bare rubrene single crystal (Fig. 4.1b) since these spectra will be instructive for the understanding of the response of rubrene-based field-effect transistors. The sharp absorption lines below

5000 cm^{-1} originate from phonons. The abrupt suppression of T(ω) at about 18000 cm^{-1} is due to the gap between HOMO and LUMO (lowest unoccupied molecular orbital) bands. The gap probed by IR, the phonon frequencies and the overall transmission level are all anisotropic within the ab-plane.

Fig. 4.1a depicts the $T(\omega,V_{GS})/T(\omega,V_{GS}=0V)$ spectra for a representative OFET at 300K, obtained with the **E** vector along the a-axis and b-axis. Similar spectral characteristics were found in all devices we investigated. Under an applied gate voltage, a pronounced suppression of the transmission of the transistor is observed. The effect is stronger for the polarization of the **E** vector along the b-axis of the rubrene single crystal. The voltage-induced changes of the transmission are most prominent at far-IR frequencies and are peaked near 400 cm^{-1}. The form of $T(V_{GS})/T(0V)$ traces does not appreciably change with the applied voltage, whereas the magnitude varies nearly linearly with V_{GS}. These observations suggest that the changes of IR properties of our devices are intimately related to the formation of ALs both in the channel of the OFET and in the ITO gate electrode. Using IR microscopy [4] we have verified that the density of induced carriers is uniform along the channel of the OFETs studied here. Therefore, the two dimensional (2D) carrier density $\boldsymbol{n_{2D}}$ in our OFETs can be estimated as follows:

$$\boldsymbol{en_{2D} = C_t V_{GS}} \qquad (4.1)$$

where e is the elementary charge.

In order to extract the *optical constants* of the electric-field-induced accumulation layer at the rubrene-parylene interface, we employ an analysis protocol

that takes into account properties of 5 layers in our devices: 1) ITO, 2) accumulation layer at the ITO-parylene interface characterized with the 2D conductivity $\Delta\sigma\ (\omega)$, 3) parylene, 4) accumulation layer at the rubrene-parylene interface with the 2D conductivity $\Delta\sigma\ (\omega)$ and 5) the bulk of rubrene crystal. The response of layers 1, 3 and 5 was assumed to be voltage independent whereas layers 2 and 4 reveal voltage-dependent properties as indicated by raw data in Fig. 4.1 of the main text. We first evaluated the complex dielectric function $\varepsilon(\omega)=\varepsilon_1(\omega)+i\varepsilon_2(\omega)$ (related to conductivity as $\varepsilon(\omega)=1+4\pi\sigma(\omega)/\omega$) for layers 1, 3, and 5 from a combination of reflection, transmission and ellipsometric measurements, as depicted in Fig. 4.2. We then extracted $\Delta\sigma_{ITO}(\omega)$ from the Drude model: $\Delta\sigma_{ITO}(\omega)=\frac{n_{2D}e^2}{m^*}\frac{\gamma_D}{\gamma_D^2+\omega^2}$, where the relaxation rate γ_D =1300 cm^{-1} and effective mass $m^*=0.5\ m_e$ was determined from the measurements of ITO films, and carrier density n_{2D} of ITO accumulation layer was obtained from Eq. (4.1). Finally, we utilized a multi-oscillator fitting procedure [20] to account for $\Delta\sigma\ (\omega)$. In this final step the transmission of the device is calculated using standard methods for multi-layered structures taking proper account for the phase coherence of all the layer [57]. Spectra of $\Delta\sigma\ (\omega)$ extracted using this routine are presented in Fig. 4.2, whereas the $T(V_{GS}=-280V)/T(0V)$ spectra generated from the multilayer model are plotted in Fig. 4.1a with thick gray lines. Alternatively the response of our devices can be described by Eq. (3) in Ref. [58], which directly relates the raw $T(V_{GS})/T(0V)$ data to the 2D conductivity of the ALs. The $\Delta\sigma\ (\omega)$ spectra inferred from these two methods are in agreement within an accuracy of 10 %, which is

comparable to the error in the raw data. It is instructive to omit the rubrene AL from the model to display the contribution of $\Delta\sigma\ (\omega)$ in the raw $T(V_{GS})/T(0V)$ (dashed line in Fig. 4.1a). This calculation shows that voltage-induced changes of the electron density in ITO result in a measurable change in the transmission. Note that the contribution of ITO to the $T(V_{GS})/T(0V)$ spectra has monotonic frequency dependence in contrast to the non-monotonic form of the overall transmission change of the device.

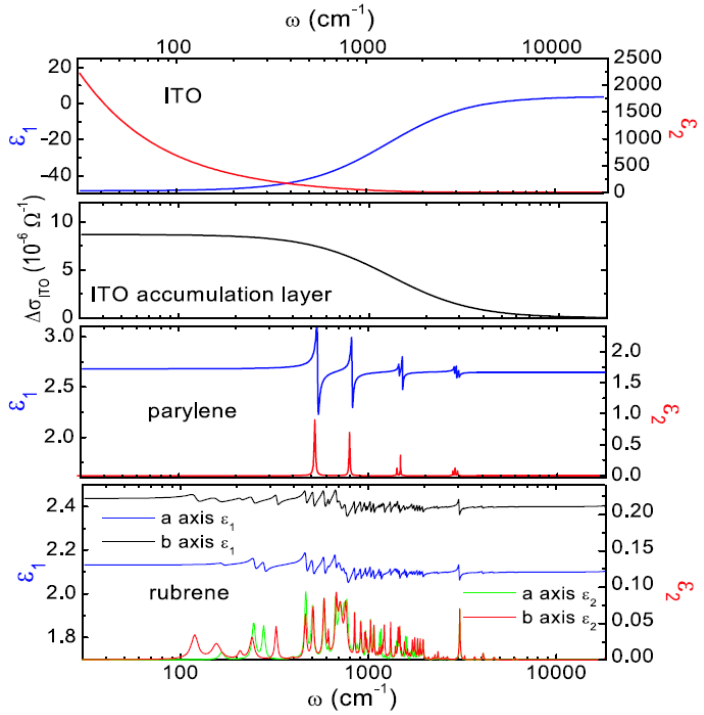

Figure 4.2: Optical constants of all constituent layers in rubrene OFETs including the conductivity of the ITO accumulation layer $\Delta\sigma_{ITO}(\omega)$ at V_{GS}=-280V.

Fig. 4.3 displays the optical conductivity spectra of the 2D system of field-induced quasiparticles at the rubrene-parylene interface $\Delta\sigma\ (\omega)$ for the polarization of the **E** vector along the a and b axes at several gate voltages. Similar to the raw

$T(V_{GS})/T(0V)$ data, the conductivity spectra are characterized by a finite energy peak centered at around 400 cm^{-1}. At frequencies below this peak, $\Delta\sigma(\omega)$ decreases toward the DC value which has been obtained independently in DC transport measurements. In the near-IR range, $\Delta\sigma(\omega)$ is negligibly small as shown in Fig. 4.1a. In particular, no noticeable features were observed in $\Delta\sigma(\omega)$ at frequencies close to the band gap of rubrene. The anisotropy of the conductivity spectra is found throughout the IR range and extends to the DC limit. Importantly, $\Delta\sigma(\omega)$ remains finite with the temperature decreasing down to 30 K (not shown) throughout the entire IR range down to at least 80-90 cm^{-1}. We therefore conclude that no sizable energy gap opens up in the IR response of the AL formed by voltage-induced holes in rubrene.

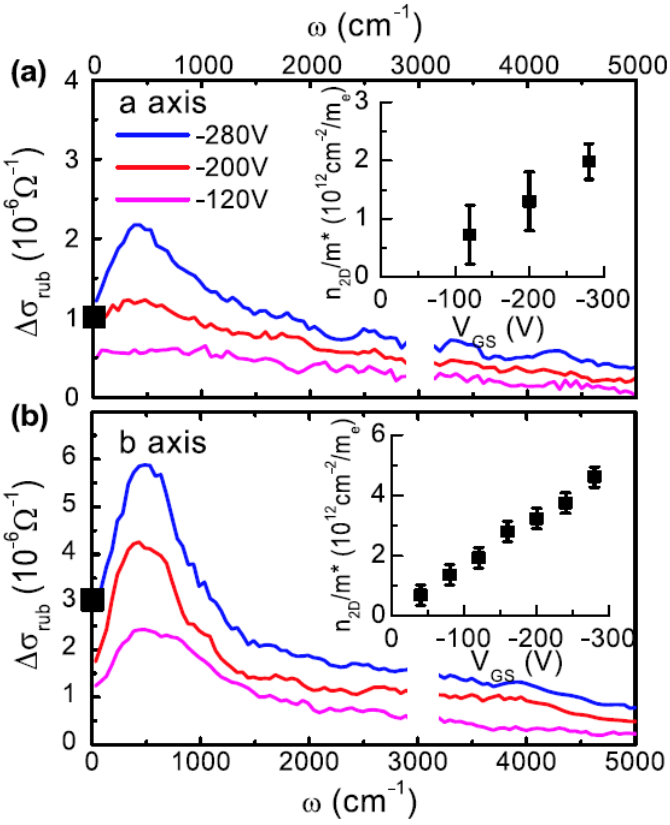

Figure 4.3: The optical conductivity of the two-dimensional system of field-induced charges on the rubrene-parylene interface $\Delta\sigma\ (\omega)$ plotted for different values of V_{GS} at room temperature. (a): E || a-axis data. (b): E || b-axis data. Black squares on the left axes: DC conductivity at -280V. Insets: the evolution of the spectral weight n_{2D}/m^* with gate voltage V_{GS}.

The non-monotonic form of the conductivity spectra in Fig. 4.3 can be qualitatively described by the localization-modified Drude model that is commonly used to account for the IR properties of organic systems and other disordered conductors in the vicinity of the metal-insulator transition [59]. This description is not unique. We therefore will focus on the overall strength of the absorption associated with charge injection in the AL. This analysis will allow us to evaluate the optical effective

masses m* of the field-induced quasiparticles at the Fermi energy E_F using the model-independent oscillator strength sum rule [60 London, 1972 #62],

$$\frac{n_{2D}}{m^*} = \frac{2}{\pi e^2}\int_0^{\Omega_c} \Delta\sigma_{rub}(\omega)d\omega . \qquad (4.2)$$

The cutoff frequency Ω_c is chosen to be 5000 cm^{-1} to accommodate the entire energy region where voltage-induced changes are prominent. Exploring the results inferred through Eq. (4.2) we first point out that n_{2D}/m^* linearly increases with V_{GS} for both E || a and E || b data (insets in Fig. 4.3). This is in accord with Eq. (4.1) provided that the effective mass does not change within the range of applied biases. This agreement of the n_{2D}/m^* data with the capacitive model justifies the use of Eq. (4.1) for extracting the charge density in the AL, which approaches $3.7*10^{12}$ cm^{-2} at -280 V. The slopes of $n_{2D}/m^*(V_{GS})$ for the E || a and E || b measurements are different as shown in Fig. 4.3. The latter effect in conjunction with Eqs. (4.1), (4.2) yields the anisotropy of the effective mass: $m_a^* = 1.85m_e$ and $m_b^* = 0.80m_e$. The direct spectroscopic observation of the mass anisotropy elucidates the origin of the direction dependence of the electronic mobility $\mu = e\tau/m^*$ discovered through transport measurements [52-55]. Indeed the magnitude of the anisotropy of m* is in good agreement with that of the mobility within experimental errors; this suggests that the anisotropic effective masses of mobile quasiparticles dominate the directional dependence of transport properties.

To understand the experimental data, we have carried out first-principles density functional theory (DFT) calculations of the band structure of rubrene within the

generalized gradient approximation (GGA) [61, 62] [63] and using the experimental lattice parameters [64, 65], as displayed in Fig. 4.4. The orthorhombic unit cell contains two ab planes, each contains two inequivalent rubrene molecules, separated by half-unit cell in the c direction. We find however that the interactions between the ab planes in the unit cell are negligible. From fitting the top of the HOMO band with parabolic functions over different energy ranges along the Γ-X and the Γ-Y directions, we obtained effective masses in the range of values $1.9\boldsymbol{m_e}<m_a<2.8\boldsymbol{m_e}$ and $1.0\boldsymbol{m_e}<m_a<1.3\boldsymbol{m_e}$ for hole carriers along the a and b directions, respectively. The DFT-GGA functional may also contribute to errors in the computed band masses. Nevertheless, the band mass values are overall comparable to those of the field-induced quasiparticles inferred from IR measurements. The difference between the two could be due to the errors in these quantities as discussed above. Therefore, our IR study, along with band structure calculations, reveals no significant enhancement of the effective mass of the quasiparticles in rubrene OFETs compared to the band values.

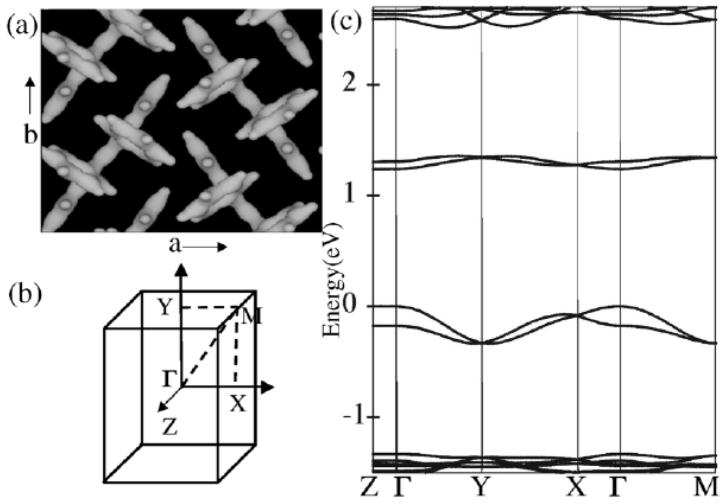

Figure 4.4: (a) The charge density isosurface enclosing 40% of the total charges obtained from DFT, which illustrates the crystal structure in the *ab* plane with two inequivalent rubrene molecules arranged in a herringbone structure. (b) The reciprocal lattice; Γ-*X*, Γ -*Y*, and Γ -*Z* correspond to the *a*, *b*, and *c* crystalline direction. (c) The band structure of rubrene calculated using DFT-GGA.

Experimental studies of charge dynamics in rubrene OFETs augmented with the analysis of the electronic structure unveil several unexpected aspects of the quasiparticles in these systems. First, no low-energy gap in the optical conductivity $\Delta\sigma(\omega)$ is observed over the whole IR range suggesting that the field-induced quasiparticles reside in a continuum of electronic states extending both above and below the Fermi energy. The states involved in quasiparticle dynamics reflect the intrinsic electronic structure of rubrene with rather distinct values of overlap integrals in the a- and b-directions. This conclusion is attested by the anisotropy of transport properties, IR conductivity and most importantly by the effective masses directly determined from the spectroscopic data. Rather small values of effective masses of mobile quasiparticles once again point to the involvement of band states (within the HOMO band) in the

electronic response in accord with the band structure analysis. These findings suggest that the periodic potential of the molecular crystal lattice and the electronic band structure play a dominant role in charge dynamics even at room temperature. Because organic molecular crystals are periodic systems, the concept of energy bands in these systems at sufficiently low temperatures is not in dispute. However, in view of the weak inter-molecular van-der-Waals bonds in these crystals, the long-range order may be disrupted by the thermally-induced dynamic disorder [66]. Nevertheless, our results show that the band dispersion evaluated in the limit of $T \rightarrow 0$ provides an accurate account of transport and IR properties at room temperature. The notion of light quasiparticles in the HOMO band established through these findings is furthermore supported by recent observations of non-activated, diffusive charge transport on the surface of high-quality molecular crystals [52-55], also suggesting the existence of extended electronic states.

Light effective masses comparable to band values reported here have not been foreseen by theoretical models commonly postulating very strong coupling between electronic and lattice degrees of freedom in molecular solids leading to the formation of small polarons even at room temperature. Small polarons are characterized by large masses of at least several times the band mass due to the coupling with lattice [50, 51] in stark contrast with our observations. Therefore, our work indicates that polaronic effects in rubrene OFETs are weaker at room temperature than previously thought, and the charge transport can be adequately described by quasiparticles in the HOMO band. This assertion is furthermore supported by the frequency dependence of the optical conductivity. Polarons in organic systems (including OFETs) typically give rise to

broad resonances in the absorption spectra in mid-IR frequencies [4] that are not detected in our data for rubrene-based transistors. We conclude that the polaron binding energies in rubrene must be below 26 meV, the energy that corresponds to room temperature. Future work will be aimed at establishing if polaronic effects in general, and enhancement of the effective mass in particular, may be responsible for a rapid suppression of the conductivity below 140 K [54].

Note: After the publication of our paper, a recent investigation of Seebeck coefficient (thermopower, or thermoelectric power) of organic single crystal FET also suggests band-like transport in these systems [67]. Our study and the results in [67] call for major revisions of the theoretical description of charge transport in molecular crystals.

Acknowledgements: This chapter contains materials in Z.Q. Li, V. Podzorov, N. Sai, M.C. Martin, M.E. Gershenson, M. Di Ventra and D.N. Basov, "*Light Quasiparticles Dominate Electronic Transport in Molecular Crystal Field-Effect Transistors*", Phys. Rev. Lett. 99, 016403 (2007). The dissertation author was the primary investigator and author of this paper. The coauthors of this paper all contribute to the studies describe in this chapter.

5

Dirac charge dynamics in graphene by infrared spectroscopy

A remarkable manifestation of the quantum character of electrons in matter is offered by graphene, a single atomic layer of graphite (Fig. 5.0). Unlike conventional solids where electrons are described with the Schrödinger equation, electronic excitations in graphene are by the Dirac Hamiltonian [68, 69]. Some of the intriguing electronic properties of graphene, such as massless Dirac quasiparticles with linear energy-momentum dispersion (as shown in Fig. 5.0), have been confirmed by recent observations [70-73].

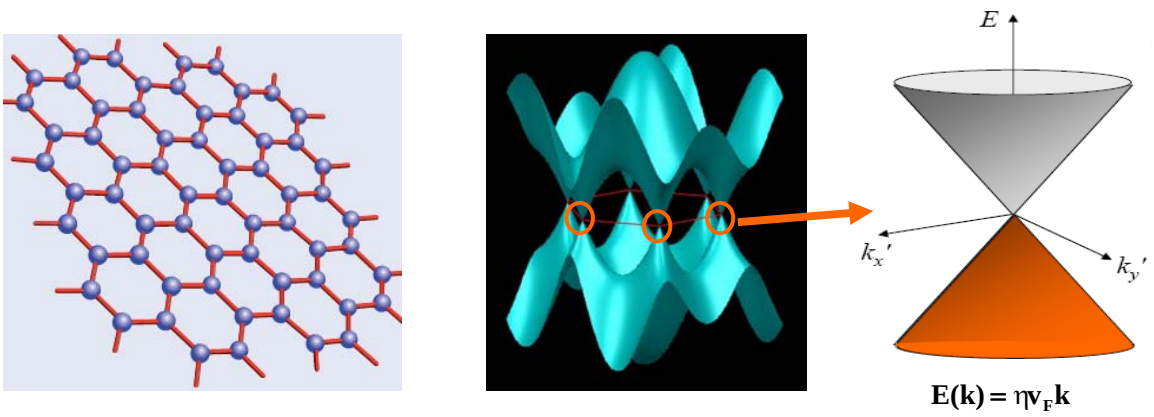

Figure 5.0: (a) A schematic of graphene: a single atomic layer of carbon atoms arranged in a honeycomb lattice. (b) The band structure of graphene $E(k_x, k_y)$ calculated from a tight binding model based on the atomic structure in (a) [68]. Intrinsic graphene is a semi-metal or zero-gap semiconductor. The E-k relation is linear for low energies near the six corners of the two-dimensional hexagonal Brillouin zone, as shown in (c). v_F is the Fermi velocity, which is the slope of the bands. Due to the linear dispersion, electrons and holes in graphene behave like Dirac quasiparticles [70-73].

Here we report an infrared (IR) spectromicroscopy study of charge dynamics in graphene integrated in gated devices. Our measurements verify the expected characteristics of graphene and, owing to the previously unattainable accuracy of IR experiments, also uncover significant departures of the quasiparticle dynamics from predictions made for Dirac fermions in idealized, free standing graphene. Several observations reported here indicate the relevance of many body interactions to the electromagnetic response of graphene.

We investigated the reflectance $R(\omega)$ and transmission $T(\omega)$ of graphene samples on a SiO_2/Si substrate (inset of Figure 5.1(a)) as a function of gate voltage V_g at 45K (see Methods). We start with data taken at the charge neutrality point V_{CN}: the

gate voltage corresponding to the minimum DC conductivity and zero total charge density (inset of Fig. 5.1(c)). Figure 5.1(a) depicts R(ω) of a graphene gated structure (graphene/SiO_2/Si) at V_{CN}=3V normalized by reflectance of the substrate $R_{sub}(\omega)$. $R_{sub}(\omega)$ is dominated by a minimum around 5500 cm^{-1} due to interference effects in SiO_2. A remarkable observation is that a monolayer of undoped graphene dramatically modifies the interference minimum of the substrate leading to a suppression of $R_{sub}(\omega)$ by as much as 15%. This observation is significant because it allows us to evaluate the conductivity of graphene near the interference structure, as will be discussed below.

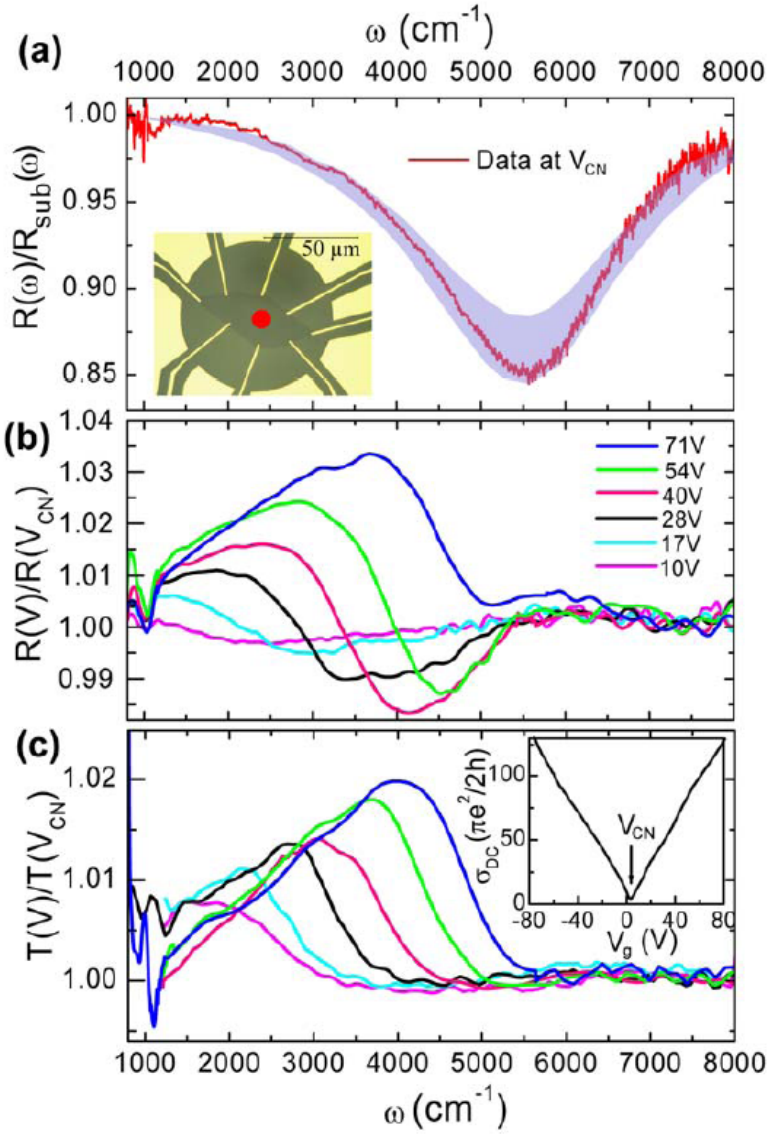

Figure 5.1: The reflectance R(ω) and transmission T(ω) of a graphene device under applied gate voltages. (a): the reflectance of the graphene device (graphene/SiO_2/Si) R(ω) normalized by that of the SiO_2/Si substrate $R_{sub}(\omega)$ at the charge neutrality voltage V_{CN}. A set of $R(\omega)/R_{sub}(\omega)$ spectra generated from the multilayer model using a constant $\sigma_1(\omega, V_{CN})$ in the range of $(1\pm0.15)\pi e^2/2h$ are shown as shaded area. The upper and lower boundary of the shaded area are defined by $\sigma_1(\omega, V_{CN})$ with values of $0.85*\pi e^2/2h$ and $1.15*\pi e^2/2h$, respectively. Inset of (a): a photograph of a graphene device together with a schematic of the focused synchrotron beam (red dot). (b) and (c): $R(V)/R(V_{CN})$ and $T(V)/T(V_{CN})$ spectra of the graphene device at several voltages corresponding to E_F on the electron side, where $V= V_g - V_{CN}$. Inset of (c): the smoothed DC conductivity data of the sample as a function of gate voltage Vg.

Both reflectance and transmission spectra of graphene structures can be modified by a gate voltage. Figure 5.1 (b) and (c) display these modifications at various gate voltages normalized by data at V_{CN}: $R(V)/R(V_{CN})$ and $T(V)/T(V_{CN})$, where $V = V_g - V_{CN}$. These data correspond to the Fermi energy E_F on the electron side and similar behavior was observed with E_F on the hole side (not shown). At low voltages (<17V) we found a dip in $R(V)/R(V_{CN})$ spectra. With increasing bias this feature evolves into a peak-dip structure and systematically shifts to higher frequency. The $T(V)/T(V_{CN})$ spectra reveal a peak at all voltages, which systematically hardens with increasing bias. A voltage-induced increase in transmission ($T(V)/T(V_{CN})>1$) signals a decrease of the absorption with bias. Most interestingly, we observed that the frequencies of the main features in $R(V)/R(V_{CN})$ and $T(V)/T(V_{CN})$ all evolve approximately as $\sqrt{V}$.

In order to explore the quasiparticle dynamics under applied voltages, it is imperative to discuss first the two dimensional (2D) optical conductivity of charge neutral graphene, $\sigma_1(\omega,V_{CN})+i\sigma_2(\omega,V_{CN})$, extracted from a multilayer analysis of the devices (see Methods). Theoretical analysis [74-76] predicts a constant "universal" 2D conductivity $\sigma_1(\omega,V_{CN})=\pi e^2/2h$ for ideal undoped graphene. Our $R(\omega)/R_{sub}(\omega)$ data are consistent with this prediction. Fig. 5.1(a) shows a comparison between experimental $R(\omega)/R_{sub}(\omega)$ spectrum and model spectra generated assuming constant $\sigma_1(\omega,V_{CN})$ values. The constant universal conductivity offers a good agreement (within ±15%) with the experimental spectra in the range 4000-6500 cm^{-1}. Outside of this spectral region, our IR measurements do not allow us to unambiguously determine the absolute value of $\sigma_1(\omega, V_{CN})$; therefore the uncertainty of $\sigma_1(\omega,V_{CN})$ increases as shown by the

shaded region weighted around the $\pi e^2/2h$ value. However, recent IR studies of graphene revealed a constant conductivity $\sigma_1(\omega, V_{CN}) = \pi e^2/2h$ between 2400 and 24000 cm^{-1} (Ref. [77] and Mak, K.F. & Heinz, T. 2008 APS March Meeting, Abstract: L29.00006, unpublished). The universal conductivity is only weakly modified in bulk highly ordered pyrolytic graphite [78] (HOPG) and extends down to 800 cm^{-1}. Thus in the following discussion, we will assume $\sigma_1(\omega, V_{CN}) = \pi e^2/2h$ throughout the entire range of our data.

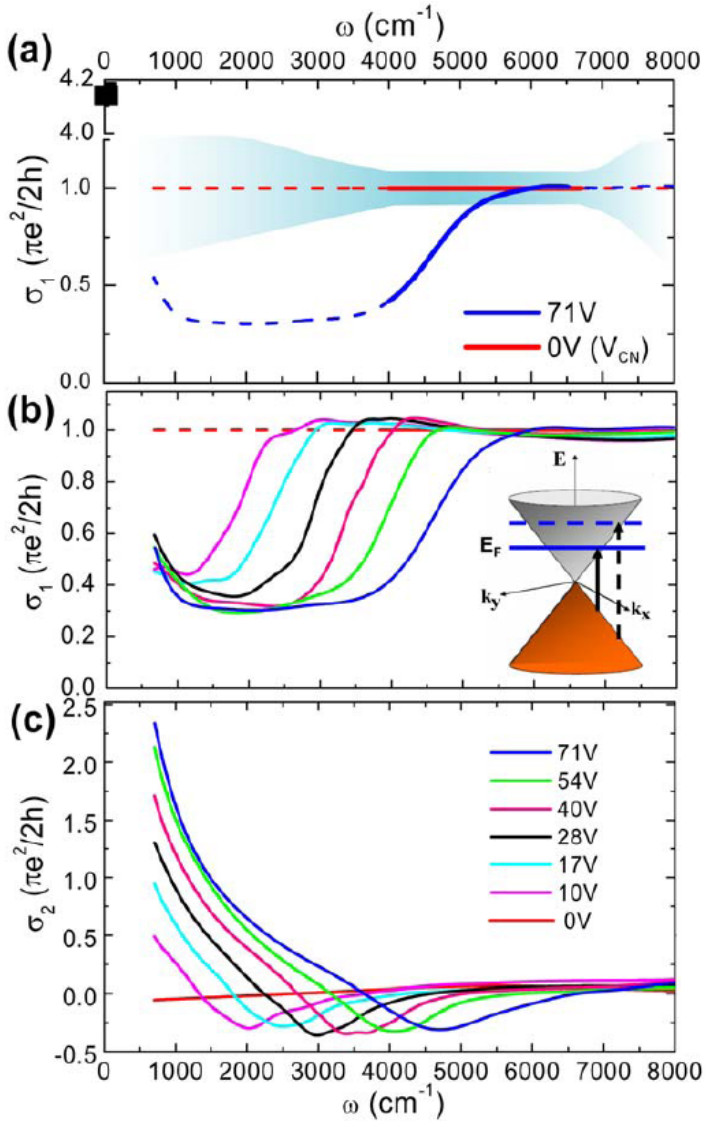

Figure 5.2: The optical conductivity of graphene at different voltages. (a), the real part of the 2D optical conductivity $\sigma_1(\omega)$ at V_{CN} and 71V. The solid red line displays the region where our data support the universal result. The uncertainty of $\sigma_1(\omega, V_{CN})$ is shown by the shaded area with the theoretical $\sigma_1(\omega)=\pi e^2/2h$ plotted as dashed line. The blue dashed line is $\sigma_1(\omega)$ at 71V evaluated for the theoretical spectra: $\sigma_1(\omega, V_{CN})= \pi e^2/2h$ (red dashed line). The key spectral features of $\sigma_1(\omega, V)$ are independent of uncertainties in $\sigma_1(\omega, V_{CN})$ indicated by the shaded area, as discussed in the text. Black square on the left axis: DC conductivity at V_{CN}. (b) and (c), $\sigma_1(\omega)$ and $\sigma_2(\omega)$ of graphene at several voltages with respect to V_{CN} corresponding to E_F on the electron side based on $\sigma_1(\omega, V_{CN})=\pi e^2/2h$. The absolute values of the $\sigma_2(\omega)$ spectra in (c) have uncertainties due to the uncertainties of $\sigma_1(\omega, V_{CN})$ as discussed in the text. Inset of (b), the band structure of graphene near the Dirac point and the interband transition at $2E_F$.

Electrostatic doping of graphene introduces two fundamental changes in the optical conductivity $\sigma_1(\omega,V)+i\sigma_2(\omega,V)$: a strong Drude component formed in the far-IR with $\sigma_1(\omega\text{--}\text{->}0)$=4-100 $\pi e^2/2h$ accompanied by a shifting of the onset of interband transitions at $2E_F$, as schematically shown in the inset of Fig. 5.2(b). In order to investigate these effects, we obtained $\sigma_1(\omega,V)+i\sigma_2(\omega,V)$ (Fig. 5.2 (b,c)) from voltage-dependent reflectance and transmission spectra (see Methods). The key features in the conductivity spectra are independent of uncertainties in $\sigma_1(\omega, V_{CN})$ discussed above. Regardless of the choice of $\sigma_1(\omega, V_{CN})$, under applied biases we observe a suppression of the conductivity compared to $\sigma_1(\omega, V_{CN})$ and a well-defined threshold structure above which the conductivity recovers the universal value $\pi e^2/2h$. The energy of the threshold structure systematically increases with voltage, a natural expectation for a transition occurring at $2E_F$. With a scattering rate $1/\tau$=30cm^{-1} at 71V independently obtained from transport data, the Drude mode is rather narrow and confined below the low-ω cut-off of our measurements. We stress that the two voltage-induced transformations of the conductivity, the intraband mode and the onset of interband absorption at $2E_F$, are interdependent as suggested by our data. Indeed, assuming the intraband component can be described with a simple Drude formula $\boldsymbol{\sigma_1(\omega) = \sigma_{DC}/(1+\omega^2\tau^2)}$ using σ_{DC} and $1/\tau$ obtained from transport measurements, we find that the spectral weight removed from $\omega<2E_F$ is recovered under the Drude structure, such that the total oscillator strength given by $\int_0^{\Omega_c}\sigma_1(\omega)d\omega$ is conserved at any bias with a cutoff frequency Ω_c=8000 cm^{-1}.

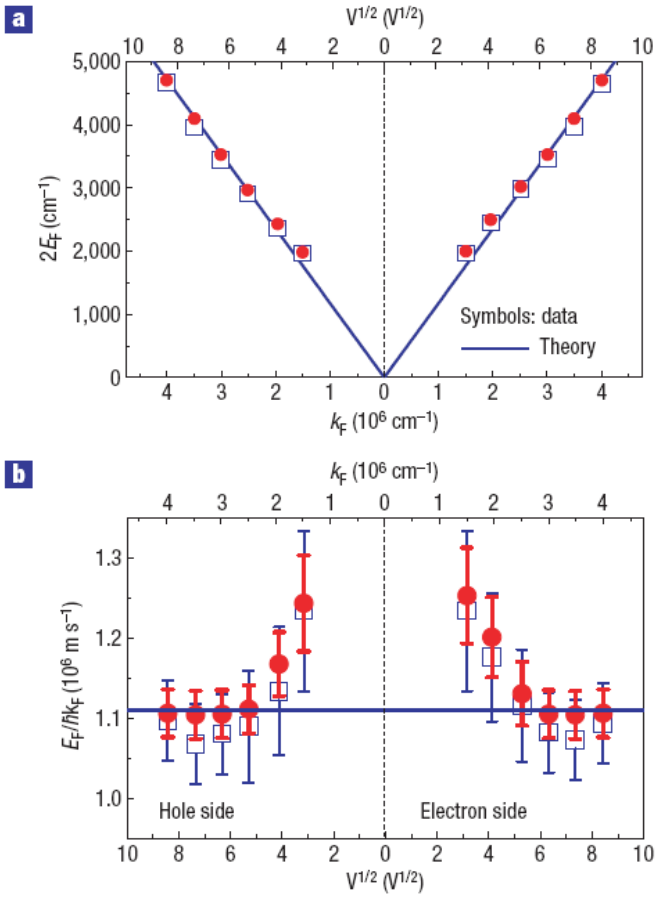

Figure 5.3: The Fermi energy E_F and the ratio of E_F to the Fermi wave vector $E_F/\eta k_F$. The magnitude of $E_F/\eta k_F$ is closely related to the Fermi velocity v_F as discussed in the text**.** (a), The magnitude of $2E_F$ plotted as a function of $V^{1/2}$ and k_F for the electron and hole sides with respect to the charge neutrality voltage. Red solid symbols: $2E_F$ extracted from the minimum in the $\sigma_2(\omega,V)$ spectra. Blue open symbols: $2E_F$ extracted from the center of the $2E_F$ threshold in $\sigma_1(\omega, V)$. The uncertainties of the $2E_F$ values discussed in the Methods section do not exceed the size of the symbols. Solid lines are theoretical $2E_F$ values using v_F=1.11*10^6 m/S. (b), Symbols: $E_F/\eta k_F$ as a function of $V^{1/2}$ and k_F. Blue line corresponds to a v_F value of 1.11*10^6 m/S. The error bars reflect uncertainties in the determination of the Fermi energy $2E_F$ from the conductivity data $\delta(E_F)$ discussed in the Methods section and are calculated as $\delta(E_F/\eta k_F)=\delta(E_F)/(\eta\sqrt{\pi C_g V/e})$.

Next we extracted Fermi energy values from the $2E_F$ threshold using two different methods (see Methods). We found that the $2E_F$ values (Fig. 5.3(a)) are

symmetric for biases delivering either holes or electrons to graphene. Moreover, $2E_F$ increases with voltage approximately as $\sqrt{V}$ (deviations from the square root law at small biases will be discussed below). Note that E_F of Dirac fermions scales with the 2D carrier density N as $E_F = \eta v_F \sqrt{\pi N}$, where v_F is the Fermi velocity. In our devices, $N = C_g V / e$ where C_g=115aF/μm^2 is the gate capacitance per unit area. Therefore, the observed $\sqrt{V}$ dependence of $2E_F$ substantiates that graphene samples integrated in gated devices are governed by Dirac quasiparticles.

Interestingly, the $2E_F$ threshold in $\sigma_1(\omega, V)$ shows a width of about 1400 cm^{-1} that is independent of gate voltage and therefore of carrier density N, irrespective of a seven-fold enhancement of N between 10V and 71V. This effect is much stronger than the theoretical estimate for thermal smearing of the $2E_F$ feature at 45K[7,8], which is about 500 cm^{-1}. A recent theoretical study [79] showed that disorder effects and electron-phonon coupling are needed to account for the width of the $2E_F$ threshold in our data. Apart from that, a spatial variation of local E_F values observed in graphene on SiO_2/Si substrates (Ref. [80] and Brar, V. et al., 2008 APS March Meeting, Abstract: U29.00003, unpublished) will inevitably lead to a broadening of the absorption onset at $2E_F$ in $\sigma_1(\omega)$, because IR measurements register the absorption averaged over a large area (a few microns in our experiments). The origin of the inhomogeneity of E_F in graphene is still an open question [80], which needs to be explored using spatially resolved probes such as near field IR conductivity studies capable of probing the response of a material with nanometer resolution over a large area [81].

Our study has uncovered several new properties of graphene that are beyond the ideal Dirac fermion picture [82]. First, our study revealed unexpected features of $\sigma_1(\omega, V)$ below $2E_F$. The band structure of ideal graphene implies that the interband transition at $2E_F$ is the lowest electronic excitation in the system apart from the Drude response at $\omega=0$. Therefore, one anticipates finding $\sigma_1(\omega,V)\approx 0$ up to the $2E_F$ threshold, provided the Drude scattering rate is much smaller than $2E_F$. This latter condition is fulfilled for all data in Fig. 5.2, and yet we registered significant conductivity below $2E_F$ (see supplementary information). This result has not been anticipated by theories developed for Dirac Fermions [74-76]. Both extrinsic and intrinsic effects may give rise to the residual conductivity in Fig. 5.2. Among the former, charged impurities and unitary scatterers (edge defects, cracks, vacancies, etc) were shown to induce considerable residual conductivity below $2E_F$ [79]. However, the theoretical residual absorption in Ref. [79] is systematically suppressed with voltage, whereas this suppression was not observed in our data. In addition, the magnitude of the theoretical residual absorption is smaller compared to experimental values in Fig. 5.2. Therefore, it is likely that other mechanisms are also responsible for the residual conductivity in our data. One intriguing interpretation of the residual conductivity is in terms of many body interactions, which are known to produce a strong frequency dependent quasiparticle scattering rate $1/\tau(\omega)$. It is predicted theoretically that $1/\tau(\omega)$ in graphene increases with frequency due to electron-electron [83, 84] and electron-phonon interactions [85]. The energy dependent scattering rate initiates a marked enhancement of the conductivity compared to the Lorentzian form prescribed by the Drude model. Such an enhancement in mid-IR frequencies has been observed in many systems [86-88].

A closer inspection of the voltage dependence of the $2E_F$ feature uncovers marked departures from the behavior anticipated within a single particle picture of graphene. In order to highlight these deviations, we plot $2E_F$ as a function of the Fermi wave vector k_F based on $k_F = \sqrt{\pi N} = \sqrt{\pi C_g V / e}$, as displayed in Fig. 5.3(a). The $E_F(k_F)$ plot has a clear physical meaning: it is a direct representation of the band dispersion. We then examine the ratio $E_F / \eta k_F$ that is directly related to the Fermi velocity v_F. The $E_F / \eta k_F$ plot as a function of $V^{1/2}$ and k_F in Fig. 5.3(b) reveals a departure from linear dispersion with a single value of $E_F / \eta k_F$ expected within a single particle picture. Moreover, $E_F / \eta k_F$ increases systematically with decreasing k_F values compared to that at high k_F values. The observed systematic enhancement of $E_F / \eta k_F$ at low k_F is indicative of many body interactions [82, 89, 90]. Signatures of band renormalization were also observed in a previous magneto-optical study of graphene [72]. Importantly, even the smallest $E_F / \eta k_F$ values in Fig. 5.3(b) are higher than that of the bulk graphite [91] (~$0.9*10^6$ m/S), which also supports the hypothesis of $E_F / \eta k_F$ renormalization in graphene. Complimentary information on the $E_F / \eta k_F$ renormalization in graphene can be obtained from photoemission, which is another potent probe of many body effects in solids. Currently available photoemission data were all collected for epitaxial graphene grown on SiC [92, 93]. This complicates a direct comparison with IR results for exfoliated samples on SiO_2/Si substrates reported here. We conclude by noting that the strong deviations of the experimental electromagnetic response from a simple single particle picture of graphene reported in our study challenge current theoretical

conceptions of fundamental properties of this interesting form of carbon and also have implications for its potential applications in opto-electronics.

Note: After the submission of our paper, we became aware of another work on gate tunable infrared properties of graphene [94].

5.A Methods:

Sample fabrication and infrared measurements

In the graphene devices studied here, monolayer graphene mechanically cleaved from Kish graphite was deposited onto an IR transparent SiO_2(300nm)/Si substrate [70, 71], which also serves as the gate electrode. Then standard fabrication procedures were used to define multiple Cr/Au (3/35 nm) contacts to the sample. The devices studied here exhibit mobility as high as 8700 $cm^2\ V^{-1}\ s^{-1}$ measured at carrier densities of $\sim 2*10^{12}\ cm^{-2}$. The characteristic half-integer quantum Hall effect is observed in these samples [70, 71] confirming the single layer nature of our specimen. IR experiments were carried out using an IR microscope operating with synchrotron source at the Advanced Light Source (ALS) in the frequency range of 700-8000 cm^{-1}. The synchrotron beam is focused in a diffraction limited spot, which is smaller than the sample. We measured the reflectance $R(\omega)$ and transmission $T(\omega)$ of the graphene devices as a function of gate voltage V_g with simultaneous monitoring of the DC resistivity.

Temperature of the graphene sample

Data reported here were obtained in a micro-cryostat with sample mounted on a coldfinger in vacuum. The temperature of our graphene sample is warmer than that of the coldfinger, due to thermal radiation from room temperature KBr optical windows and electrical isolation of the devices from the coldfinger that compromises thermal contact. A sensor mounted in the immediate proximity to the Si substrate of the devices read T=45 K at the lowest temperatures attainable at the coldfinger. Because both the temperature sensor and the device are in nearly identical environment, we assumed this reading to be accurate for graphene as well.

Extracting the optical constants of graphene

The graphene device contains four layers: (1) graphene with 2D optical conductivity $\sigma(\omega)= \sigma_1(\omega)+i\sigma_2(\omega)$, (2) SiO_2 gate insulator, (3) Si accumulation layer that forms at the interface of SiO_2/Si under the applied bias and (4) Si substrate. Properties of layers 2 and 4 are independent of the gate voltage whereas layers 1 and 3 are systematically modified by Vg. In our analysis of these multilayer structures we followed the protocol detailed in Reference [5]. Specifically, we carried out reflection, transmission, and ellipsometric measurements on the Si substrates and SiO_2/Si wafers used in our devices and thus obtained the optical constants of layers (2) and (4). We then investigated IR properties of test devices Ti/SiO_2/Si as a function of gate voltage and thus extracted the optical constants of the Si accumulation layer in wafers used for graphene devices. We find that the response of the Si accumulation layer is confined to far-IR frequencies [45] and gives negligible contribution to mid-IR data in Fig. 5.1. Finally, we employed a multi-oscillator fitting procedure [5] to account for the

contribution of $\sigma(\omega)$ of graphene to the reflectance and transmission spectra shown in Fig 5.1 using standard methods for multilayered structures.

Extracting Fermi energy E_F from conductivity spectra

Because of the broadening of the $2E_F$ threshold in $\sigma_1(\omega,V)$, the E_F values can be determined most accurately from the imaginary part of the optical conductivity spectra $\sigma_2(\omega,V)$ depicted in Fig. 5.2(c). Indeed, these spectra reveal a sharp minimum at $\omega=2E_F$ in agreement with previous theoretical prediction [95]. The minimum in $\sigma_2(\omega,V)$ spectrum is found from the frequency where the derivative of $\sigma_2(\omega,V)$ with respect to frequency is zero. The uncertainties of $2E_F$ obtained from this method are related to the accuracy in defining the minimum in $\sigma_2(\omega,V)$ spectrum. Alternatively, $2E_F$ values can be extracted from the center frequency of the $2E_F$ threshold in $\sigma_1(\omega, V)$. The second method has larger uncertainties as shown in Fig. 5.3, due to the ambiguity of defining the center of the $2E_F$ threshold in $\sigma_1(\omega, V)$.

5.B Supplementary Information

Spectral features in the raw reflectance/ transmission data and their connection to the broadening of the $2E_F$ threshold and residual absorption of graphene.

As discussed in the text, our study has uncovered an anomalous width of the $2E_F$ threshold and a strong residual absorption below $2E_F$ in the conductivity spectra of monolayer graphene. It is straightforward to relate both effects to features in the raw

data. In Fig. 5.4 we compare the raw R(V)/R(V_{CN}) and T(V)/T(V_{CN}) spectra (blue curves) with similar spectra generated from a model $\sigma_1(\omega)$ spectrum for ideal graphene (black curves). The top panel details the input for these model calculations. In this panel we plot with the black line the conductivity of ideal graphene $\sigma_1(\omega)$ obtained using an analytical expression for the optical constants of graphene derived by Gusynin et al. [96]:

$$\sigma_1(\Omega) = \frac{e^2 N_f}{2\pi^2 \eta}\int_{-\infty}^{\infty} d\omega \frac{[n_F(\omega) - n_F(\omega')]}{\Omega}\frac{\pi}{4\omega\omega'}\left[\frac{2\Gamma(\omega)}{\Omega^2 + 4\Gamma^2(\omega)} - \frac{2\Gamma(\omega)}{(\omega+\omega')^2 + 4\Gamma^2(\omega)}\right](|\omega| + |\omega'|)(\omega^2 + \omega'^2)$$

where $\omega' = \omega + \Omega$, $n_F(\omega) = \frac{1}{e^{(\omega - E_F)/T} + 1}$ is the Fermi distribution, $N_f = 2$ is the spin degeneracy, and $\Gamma(\omega)$ is an impurity scattering rate. A constant scattering rate Γ is used in the theoretical formula. In order to facilitate comparison with our mid-IR data, we have set the Fermi energy $2E_F$=5600 cm^{-1}. By setting the scattering rate to Γ=1 cm^{-1} and temperature to T=45 K, we are able to model the threshold structure at $2E_F$ influenced by thermal broadening representing experimental conditions. We utilized the above equation in the interband region and in order to account for the free carrier response we augmented this result with the Drude Lorentzian $\sigma_1(\omega) = \sigma_{DC}/(1 + \omega^2\tau^2)$, where σ_{DC}=100* $\pi e^2/2h$ and a scattering rate $1/\tau$=30cm^{-1} is obtained from the transport data for our device. The model R(V)/R(V_{CN}) and T(V)/T(V_{CN}) spectra were calculated based on the input $\sigma_1(\omega, V_{CN})$ spectrum in Fig. 5.4(a) using the procedure described in the Methods section. The dip-peak feature around 1000 cm^{-1} in all the experimental and model spectra in Fig. 5.4(b, c) is due to a phonon of SiO_2. Vertical dashed lines in the

plot show that the width $\delta 2E_F$ of the interband threshold in $\sigma_1(\omega)$ is determined by broadening of the high frequency edge in $T(V)/T(V_{CN})$. Furthermore, this connection was validated through calculations using different values of the phenomenological damping constant Γ. Thus with the guidance provided by modeling results in Fig.5.4 one can read the broadening of the $2E_F$ feature directly from the $T(V)/T(V_{CN})$ data and conclude that $\delta 2E_F \approx 1400$ cm^{-1} at all biases.

Model spectra are equally helpful for substantiating significant residual conductivity of graphene below the $2E_F$. For this purpose it is instructive to analyze the upper limit of the $T(V)/T(V_{CN})$ values at $\omega=2E_F$ corresponding to the maximum depletion of the conductivity under the applied bias. Our modeling shows that this upper limit is determined by the transmission of the graphene gated structure at the charge neutrality point $T(\omega,..V_{CN})$ and the transmission of the Si substrate $T_{sub}(\omega)$ as $T(\omega,..V_{CN})/T_{sub}(\omega)$, where $T_{sub}(\omega)$ is obtained from IR measurements and $T(\omega,..V_{CN})$ is calculated from the multi-layer model using the theoretical universal conductivity $\sigma_1(\omega,..V_{CN}) = \pi e^2/2h$ for graphene. Provided the residual conductivity is vanishingly small, the peak in $T(V)/T(V_{CN})$ spectra at $\omega=2E_F$ reaches the upper boundary. Under these latter conditions the amplitude of peaks in a series of spectra generated for different biases will trace the boundary of the shaded region in Fig.5.4(b). However, if the depletion of the conductivity at $\omega<2E_F$ is incomplete, the residual absorption will reduce the amplitude of $T(V)/T(V_{CN})$ below the upper limit.. This is indeed the case for the experimental spectrum in Fig.5.4-(b) taken at V=71 V and for the entire data set in Fig. 5.1. Similarly, the amplitude of changes of reflectance is also reduced by the residual

conductivity (Fig.5.4-c). We note that deviations between experimental and model spectra is significant compared to the signal-to-noise of our measurements.

Here we stress that the magnitude of $\sigma_1(\omega, V)$ below the $2E_F$ threshold is sensitive to ambiguities with the choice of $\sigma_1(\omega, V_{CN})$. An assumption of the universal value for $\sigma_1(\omega, V_{CN})$ implies that the residual conductivity is as strong as $0.3*\pi e^2/2h$. Within limitations of our measurements we cannot unambiguously rule out $\sigma_1(\omega, V_{CN})< \pi e^2/2h$ at energies below 4000 cm^{-1} and dependent on the input for $\sigma_1(\omega, V_{CN})$ the residual values at $\omega<2E_F$ may significantly vary. Within these constrains, our data indicate either a breakdown of the universal conductivity $\sigma_1(\omega, V_{CN})= \pi e^2/2h$ or significant residual conductivity below $2E_F$ at finite doping. Note that other experimental studies [77, 78] attest to the validity of $\sigma_1(\omega, V_{CN})= \pi e^2/2h$ assumption in the entire mid-IR, which implies strong residual absorption below the $2E_F$ cut-off that is nearly independent of the applied voltage.

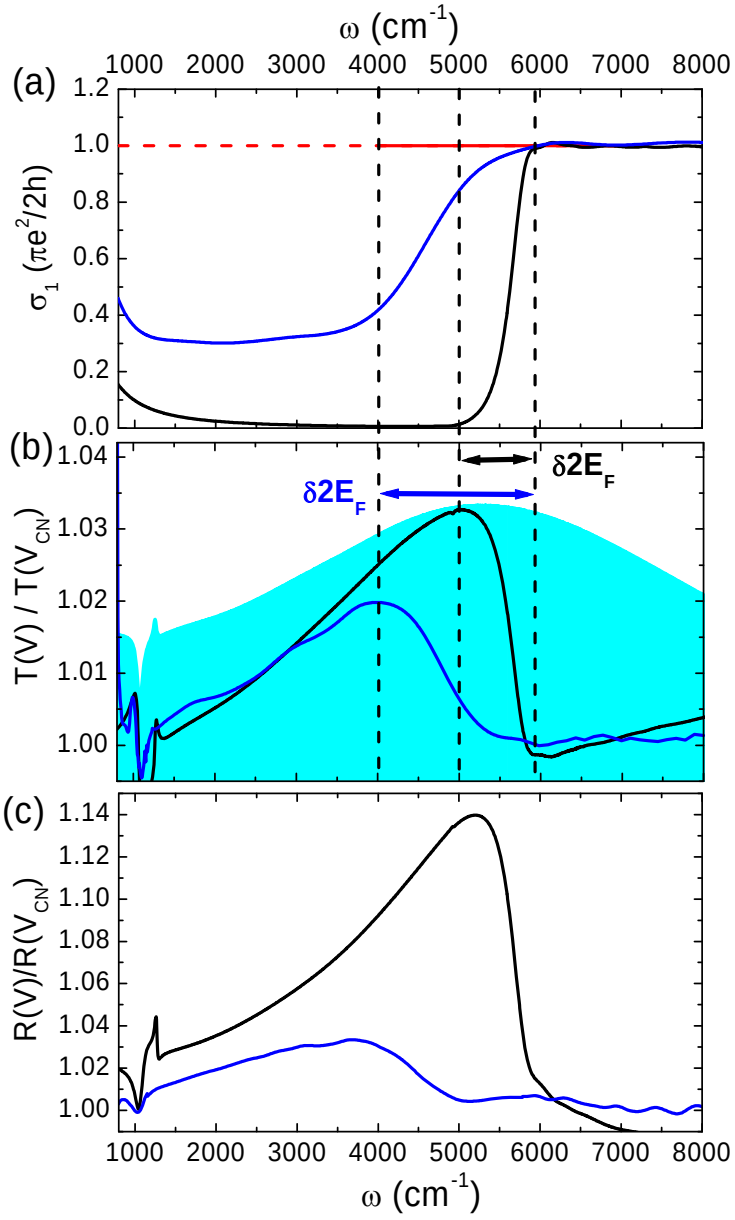

Figure 5.4: (a), the theoretical 2D optical conductivity $\sigma_1(\omega,V_{CN})$ at the charge neutrality point V_{CN} (red curve) and experimental $\sigma_1(\omega)$ spectrum at 71V (blue curve), together with a model $\sigma_1(\omega,71\ V)$ (black curve). The model spectrum reveals narrow width of the $2E_F$ threshold and negligible residual conductivity below $2E_F$. (b) and (c): experimental $R(V)/R(V_{CN})$ and $T(V)/T(V_{CN})$ spectra at 71V (blue spectra) and model data corresponding to the conductivity in (a) (black spectra). The upper boundary of the shaded region in (b) is the upper limit of $T(V)/T(V_{CN})$ values for different biases of our devices as described in the text.

Acknowledgements: This chapter contains materials in Z.Q. Li, E.A. Henriksen, Z. Jiang, Z. Hao, M.C. Martin, P. Kim, H.L. Stormer, and D.N. Basov, "*Dirac charge dynamics in graphene by infrared spectroscopy*", Nature Physics 4, 532 (2008). The dissertation author was the primary investigator and author of this paper. The coauthors of this paper all contribute to the studies describe in this chapter.

6

Band structure asymmetry of bilayer graphene revealed by infrared spectroscopy

Recently there has been unprecedented interest in carbon-based materials due to the discovery of graphene [70, 71, 82, 97, 98]. Among all carbon systems, bilayer graphene stands out due to its remarkable properties such as a unique quantum Hall effect stemming from a previously unknown type of quasiparticles, massive chiral quasiparticles [99]. Bilayer graphene is predicted to show strong many body interactions due to the unusual shape of the Fermi surface [100, 101]. Moreover, it is the only known semiconductor with a tunable band gap between the valence and conduction bands [102-108], which demonstrates its great potential for future nano-electronic applications. Therefore, it is of utmost importance to acquire a comprehensive understanding of this material in view of both fundamental research and applications. One central issue is how the Dirac quasiparticles in single layer graphene are modified when two graphene sheets are stacked together in bilayer graphene. The vast majority of previous experimental and theoretical studies have assumed that the electronic band structure of bilayer graphene taking proper account of interlayer interaction is symmetric. This is in contrast with a significant electron-hole asymmetry observed in cyclotron resonance [109] and cyclotron mass experiments [102]. Several theoretical proposals have been put forward to explain these results [102, 110].

However, our current understanding of the observed effects remains incomplete. Furthermore, the interlayer coupling energy γ_1 that controls the fundamental properties of bilayer graphene is yet to be determined [102, 111, 112].

Here we present the first investigation of the optical conductivity of bilayer graphene via infrared spectroscopy. We observed dramatic differences in the evolution of the conductivity for electron and hole polarities of the gate voltage. We show that small band parameters other than γ_1 give rise to an asymmetry between the valence and conduction bands, in contrast to the commonly assumed symmetric band structure. The systematic character of our IR data enables us to extract an energy difference between the A and B sublattices within the same graphene layer (Fig 6.1(b)) of Δ_{AB}~18meV. Moreover, the value of γ_1, ~404meV, is determined from direct measurements of interband transitions. We discuss the broad implications of these findings for the fundamental understanding of bilayer graphene.

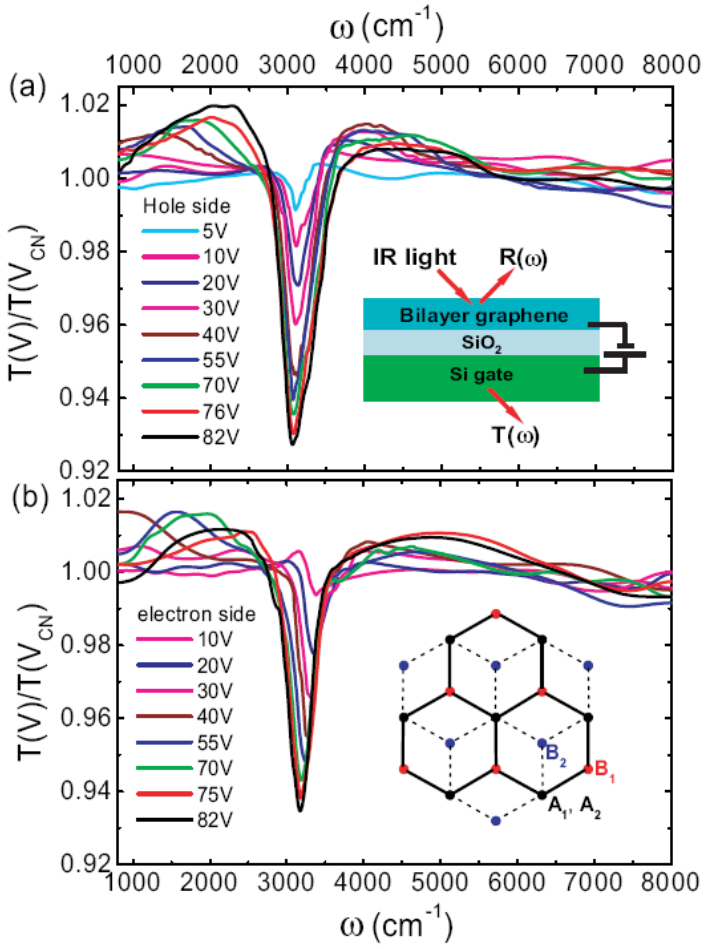

Figure 6.1: $T(V)/T(V_{CN})$ spectra of bilayer graphene. (a) and (b): data for E_F on the hole side and electron side. Inset of (a): a schematic of the device and infrared measurements. Inset of (b): a schematic of bilayer graphene. The solid lines indicate bonds in the top layer A_1B_1, whereas the dashed lines indicate bonds in the bottom layer A_2B_2. The sublattice A_1 is right on top of the sublattice A_2.

Infrared (IR) reflectance R(ω) and transmission T(ω) measurements were performed on bilayer graphene samples on SiO_2/Si substrate [109] as a function of gate voltage V_g at 45K employing synchrotron radiation, as described in [6]. We find that both R(ω) [94, 113] and T(ω) spectra of the bilayer graphene device can be strongly modified by a gate voltage. Figure 6.1 shows the transmission ratio data at several voltages normalized by data at the charge neutrality voltage V_{CN}: $T(V)/T(V_{CN})$, where

V_{CN} is the gate voltage corresponding to the minimum DC conductivity and zero total charge density, and $V= V_g - V_{CN}$. The $T(V)/T(V_{CN})$ spectra are dominated by a dip at around 3000 cm^{-1}, the magnitude of which increases systematically with voltage. Apart from the main dip, a peak was observed in the $T(V)/T(V_{CN})$ data below 2500 cm^{-1}, which shifts systematically with voltage. This latter feature is similar to the $T(V)/T(V_{CN})$ data for single layer graphene [6]. The gate-induced enhancement in transmission ($T(V)/T(V_{CN})>1$) below 2500 cm^{-1} and above 3500 cm^{-1} implies a decrease of the absorption with voltage in these frequency ranges.

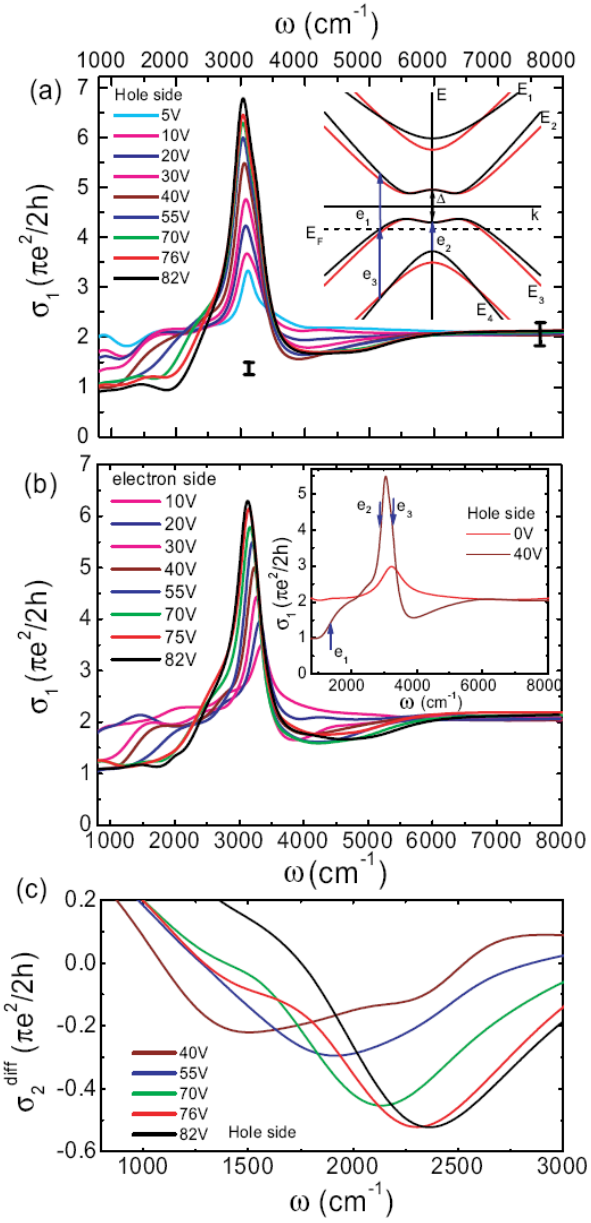

Figure 6.2: The optical conductivity of bilayer graphene. (a) and (b): $\sigma_1(\omega,V)$ data for E_F on the hole side and electron side. (c): $\sigma_2^{diff}(\omega,V)$ spectra in the low frequency range, after subtracting the Lorentzian oscillators describing the main resonacne around 3000 cm^{-1} from the whole $\sigma_2(\omega,V)$ spectra. Inset of (a): Schematics of the band structure of bilayer with zero values of Δ_{AB} and v_4 (red) and finite values of Δ_{AB} and v_4 (black), together with allowed interband transitions. Insets of (b): $\sigma_1(\omega,V)$ at 0V (V_{CN}) and 40V on the hole side with assignments of the features.

The most informative quantity for exploring the quasiparticle dynamics in bilayer graphene is the two dimensional (2D) optical conductivity $\sigma_1(\omega)+\iota\sigma_2(\omega)$ [5, 6]. First, we extracted the optical conductivity at V_{CN} from the reflectance data (not shown) employing a multilayer analysis of the device [5, 6]. We find that $\sigma_1(\omega, V_{CN})$ has a value around $2*(\pi e^2/2h)$ with a pronounced peak at 3250 cm^{-1} (inset of Fig 6.2(b)). This observation is in agreement with theoretical analysis on undoped bilayer graphene [114-117]. Our high energy data agree with recent experiments in the visible region [77]. The peak around 3250 cm^{-1} can be assigned to the interband transition in undoped bilayer near the interlayer coupling energy γ_1.

An applied gate voltage shifts the Fermi energy E_F to finite values leading to significant modifications of the optical conductivity. The $\sigma_1(\omega,V)$ and $\sigma_2(\omega,V)$ spectra extracted from voltage-dependent reflectance and transmission data [6] are shown in Fig 6.2. At frequencies below 2500 cm^{-1}, we observe a suppression of $\sigma_1(\omega,V)$ below $2*(\pi e^2/2h)$ and a well-defined threshold structure, the energy of which systematically increases with voltage. Significant conductivity was observed at frequencies below the threshold feature. These observations are similar to the data in single layer graphene [6]. The threshold feature below 2500 cm^{-1} can be attributed to the onset of interband transitions at $2E_F$, as shown by the arrow labeled e_1 in the inset of Fig 6.2(a) and (b). The observed residual conductivity below $2E_F$ is in contrast to the theoretical absorption for ideal bilayer graphene [115, 116] that shows nearly zero conductivity up to $2E_F$. Similar to single layer graphene, the residual conductivity may originate from disorder effects [115] or many body intertactions [6]. Apart from the

above similarities, the optical conductivity of bilayer graphene is significantly different from the single layer conductivity. First, the energy range where the conductivity $\sigma_1(\omega, V)$ is impacted by the gate voltage extends well beyond the $2E_F$ threshold. Furthermore, we find a pronounced peak near 3000 cm^{-1}, the oscillator strength of which shows a strong voltage dependence. This peak originates from the interband transition between the two conduction bands or two valence bands (inset of Fig. 6.2a) [115, 116].

The voltage dependence of the Fermi energy in bilayer graphene can be extracted from $\sigma_2(\omega, V)$ using a similar procedure as in [6]. In order to isolate the $2E_F$ feature, we fit the main resonance near 3000 cm^{-1} with Lorentzian oscillators and then subtracted them from the experimental $\sigma_2(\omega, V)$ spectra to obtain $\sigma_2^{diff}(\omega, V)$. The latter spectra reveal a sharp minimum at $\omega=2E_F$ (Fig 6.2(c)) in agreement with single layer graphene [6]. Figure 6.3a depicts the experimental $2E_F$ values along with the theoretical result in [104]. Assuming the Fermi velocity v_F in bilayer graphene is similar to that in single layer graphene ($v_F=1.1*10^6$ m/s), we find that our data can be fitted with $\gamma_1=450\pm80$meV. Equally successful fits can be obtained assuming the Fermi velocity and interlayer coupling in the following parameter space: $v_F=1.0\text{-}1.1*10^6$ m/s and $\gamma_1=360\text{-}450$ meV. Previous studies showed that an applied gate voltage opens a Δ between the valence and conduction bands [102-108]. Because $\Delta(V)$ is much smaller than $2E_F(V)$ for any applied bias in bottom-gate devices [104], it has negligible effects on the experimentally observed $2E_F(V)$ behavior.

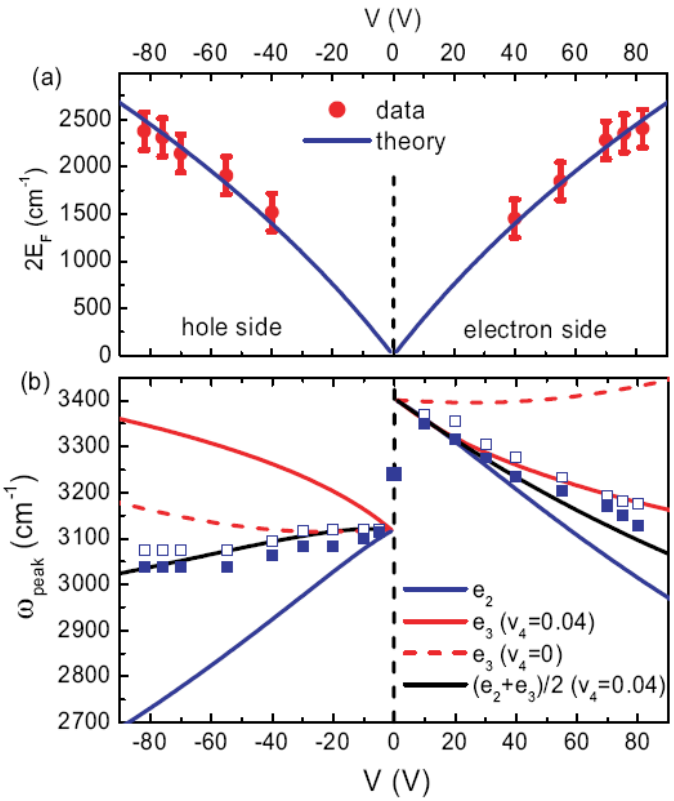

Figure 6.3: (a) Symbols: the $2E_F$ values extracted from the optical conductivity detailed in the text. The error bars are estimates of the uncertainties of $\sigma_2^{diff}(\omega,V)$ spectra in Fig 6.2(c). Solid lines: the theoretical $2E_F$ values using v_F=1.1*10^6 m/s and γ_1=450 meV. (b) Solid symbols, the energy of the main peak ω_{peak} in the $\sigma_1(\omega,V)$ spectrum. Open symbols: the energy of the dip feature ω_{dip} in the T(V)/T(V_{CN}) spectra. Note that ω_{peak} in the $\sigma_1(\omega,V)$ is shifted from ω_{dip} in the T(V)/T(V_{CN}) data with an almost constant offset, which is due to the presence of the substrate. Solid lines: theoretical values of the transitions at e_2, e_3 and (e_2+e_3)/2 with v_F=1.1*10^6 m/s, γ_1=404 meV, Δ_{AB} =18meV and v_4=0.04. Red dashed lines: e_3 with similar parameters except v_4=0.

The central result of our study is an observation of a pronounced asymmetry in evolution of the optical conductivity upon injection of electrons or holes in bilayer graphene. Specifically, the frequencies of the main peak ω_{peak} in $\sigma_1(\omega,V)$ are very distinct for E_F on the electron and hole sides, as shown in Fig 6.3(b). In addition, ω_{peak} on the electron side shows a much stronger voltage dependence compared to that on the

hole side. All these features are evident in the raw data in Fig 6.1, where the resonance leads to a dip in $T(V)/T(V_{CN})$ spectra. These behaviors are reproducible in multiple gated samples. Such an electron-hole asymmetry is beyond a simple band structure only taking γ_1 into account, which predicts symmetric properties between electron and hole sides.

The electron-hole asymmetry in our $\sigma_1(\omega,V)$ data can be explained by an asymmetry between valence and conduction bands[118]. Such an asymmetric band structure arises from finite band parameters Δ_{AB} and v_4, where Δ_{AB} (denoted as Δ in [115, 119] is the energy difference between A and B sublattices within the same graphene layer, and $v_4=\gamma_4/\gamma_0$. γ_4 and γ_0 are defined as interlayer next-nearest-neighbor coupling energy and in-plane nearest-neighbor coupling energy, respectively [115, 119]. We first illustrate the effects of Δ_{AB} and v_4 on the energy bands of bilayer graphene $E_i(k)$ (i=1,2,3,4), which can be obtained from solving the tight binding Hamiltonian Eq (6) in Ref. [115]. We find that finite values of Δ_{AB} and v_4 break the symmetry between valence and conduction bands, as schematically shown in the inset of Fig 6.2(a). Specifically, Δ_{AB} induces an asymmetry in E_1 and E_4 bands such that $E_1 > E_4$ at k=0, whereas v_4 induces an electron-hole asymmetry in the slope of the valence and conduction bands. With finite v_4, the bands E_1 and E_2 are closer and E_3 and E_4 are further apart at high k compared to those with zero v_4 value.

Next we examine the effects of Δ_{AB} and v_4 on $\sigma_1(\omega,V)$. It was predicted theoretically [116] that the 3000 cm^{-1} peak in $\sigma_1(\omega,V)$ occurs in the frequency range between two transitions labeled e_2 and e_3 as shown in the inset of Fig 6.2(a) and (b).

Here $e_2=-E_4(k=0)-\Delta/2$ and $e_3=E_3(k=k_F)-E_4(k=k_F)$ for the hole side, and $e_2=E_1(k=0)-\Delta/2$ and $e_3=E_1(k=k_F)-E_2(k=k_F)$ for the electron side [116], with Δ defined as the gap at k=0. For zero values of Δ_{AB} and v_4, e_2 and e_3 transitions are identical on the electron and hole sides. The finite values of Δ_{AB} and v_4 induce a significant inequality between e_2 and e_3 on the electron and hole sides. We first focus on the low voltage regime, where $\omega_{peak}\approx e_2\approx e_3$. Because v_F and v_4 always enter the Hamiltonian in the form of v_Fk and v_4k products [115], these terms give vanishing contributions at low V, where k goes to zero. Consequently, ω_{peak} value at low bias is solely determined by γ_1 and Δ_{AB}, with $\omega_{peak}=\gamma_1+\Delta_{AB}$ and $\omega_{peak}=\gamma_1-\Delta_{AB}$ for electron and hole side, respectively. At V_{CN} (0V), interband transitions between the two conduction bands and the two valence bands are both allowed, which leads to a broad peak centered between $\gamma_1+\Delta_{AB}$ and $\gamma_1-\Delta_{AB}$ (Fig 6.3(b)). From the two distinct low voltage ω_{peak} values on the electron and hole sides shown in Fig 6.3(b), the values of γ_1 and Δ_{AB} can be determined with great accuracy: $\gamma_1=404\pm10$meV and $\Delta_{AB}=18\pm2$meV. Therefore, the $\sigma_1(\omega,V)$ data at low biases clearly indicates an asymmetry between valence and conduction bands in bilayer graphene due to finite energy difference of A and B sublattices.

In order to explore the V dependence of ω_{peak} and the width of the main peak in $\sigma_1(\omega,V)$, Γ_{peak}, we plot the e_2 and e_3 transition energies [116] as a function of V (Fig. 6.3b), using the gap formula $\Delta(V)$ in [104] [120] and our calculated asymmetric dispersion $E_i(k)$ (i=1,2,3,4) [121], with $v_F=1.1*10^6$m/s, $\gamma_1=404$meV, $\Delta_{AB}=18$meV, and for both $v_4=0$ and $v_4=0.04$. We find that e_2 does not depend on v_4, whereas e_3 is strongly

affected by v_4. With a finite value of v_4 (~0.04), an assignment of ω_{peak} to $(e_2+e_3)/2$ appears to fit our data well on both electron and hole sides. Nevertheless, larger separation of e_2 and e_3 on the hole side is inconsistent with the relatively narrow peak in $\sigma_1(\omega,V)$ for both electron and hole injection with nearly identical width. Yet the finite value of the v_4 parameter [112] is essential to qualitatively account for the voltage dependence of ω_{peak}, because with v_4 ~0 ω_{peak} follows e_2 and e_3 on the electron and hole sides (Fig 6.3b), respectively, eluding a consistent description. A quantitative analysis of the V dependence of ω_{peak} and Γ_{peak} is discussed in [118].

We stress that γ_1 and Δ_{AB} are determined from the low bias (low k_F) data. Therefore the values of γ_1 and Δ_{AB} reported here do not suffer from the currently incomplete understanding of V dependence of ω_{peak} and Γ_{peak} discussed above. The γ_1 value (404±10meV) is directly determined from measurements of transitions between the two conduction bands or valence bands without any assumptions. This value is more accurate than previous indirect measurements of γ_1 [102, 111, 112]. The accurate determination of γ_1 is paramount since it governs the fundamental properties of bilayer such as the quantitative behavior of the tunable band gap [102, 104].

IR measurements reported here have enabled accurate extraction of Δ_{AB} (18meV) in bilayer graphene free from ambiguities of alternative experimental methods. For comparison, the energy difference between A and B sublattices Δ_{AB} in graphite is about 36meV [118, 119]. Note that, in graphite, $\Delta_{AB}=\Delta-\gamma_2+\gamma_5$, where γ_2 and γ_5 are band

parameters of graphite[118]. As pointed out in [118], Δ_{AB}(graphite) ~2 Δ_{AB}(bilayer) is exactly what one would expect within the tight binding model of graphite. The physical origin of Δ_{AB} is the short-range (exponentially decaying with distance) repulsion due to exchange and correlation effects between the electron states of the stacked atoms. (Neither Coulomb nor even the van derWaals interaction have short enough range to effectively discriminate between the two sublattices, given the relatively large interlayer distance.) Since in the bilayer each A atom has a single stacking partner while in the Bernal graphite it has two of them, one expect Δ_{AB}(graphite) ~2 Δ_{AB}(bilayer).[118]

The asymmetry between valence and conduction bands uncovered by our study has broad implications on the fundamental understanding of bilayer graphene. An electron-hole asymmetry was observed in the cyclotron resonance [109] and cyclotron mass experiments [102] in bilayer, both of which have eluded a complete understanding so far. Our accurate determination of finite values of Δ_{AB} and v_4 calls for explicit account of the asymmetric band structure in the interpretation of the cyclotron data. Moreover, the different Δ_{AB} values in bilayer graphene and graphite reveal the importance of interlayer coupling in defining the electronic properties and band structure of graphitic systems.

During the preparation of this paper, we became aware of another infrared study of bilayer graphene by A.B. Kuzmenko et al [113]. We thank M. L. Zhang and M. M. Fogler for their discussions on the theoretical interpretations of the data.

Acknowledgements: This chapter contains materials in Z.Q. Li, E.A. Henriksen, Z. Jiang, Z. Hao, M.C. Martin, P. Kim, H.L. Stormer, and D.N. Basov, "*Band structure asymmetry of bilayer graphene revealed by infrared spectroscopy*", arXiv:0807.3776 (2008), which was submitted and posted online. The dissertation author was the primary investigator and author of this paper. The coauthors of this paper all contribute to the studies describe in this chapter.

7

Charge dynamics in graphite: zero field and the extreme quantum limit

7.1 Introduction

Recent interest in electronic transport and optical properties of carbon-based materials has been prompted by the discovery of graphene, a one-atom-thick sheet of carbon [70, 71, 82, 97, 98]. The charge carriers in graphene are found to behave like relativistic Dirac quasiparticles [6, 70-72], which exhibit a spectrum of fascinating new physics [70, 71, 82, 97, 98] such as an anomalous quantum Hall effect. The low energy excitations in intrinsic (undoped) graphene are governed by interband transitions. The optical conductivity of intrinsic graphene was predicted to be a frequency independent universal value $\pi e^2/2h$ [74-76, 122] in a broad energy range below the bandwidth (~2eV) [92, 93], where energy bands with linear dispersion was found in graphene. Such a universal conductivity has been observed in a number of recent experiments [6, 77].

The universal conductivity of graphene can be significantly modified by interlayer coupling when two or more graphene layers are stacked together [115]. For instance, the optical conductivity of bilayer graphene has been predicted to show a peak around the interlayer coupling energy and many other features not present in the response of graphene [114-117]. These predictions are consistent with recent infrared

(IR) experiments on bilayer samples [7]. In bulk single crystal or highly oriented pyrolitic graphite (HOPG), graphene layers are stacked along the c-axis following one of several possible rules, most often with the Bernal stacking [119]. Therefore, the c-axis hopping is also expected to have a considerable effect on the optical conductivity. However, a recent IR study found that the sheet optical conductivity per graphene layer of HOPG is close to the universal conductivity of monolayer graphene $\pi e^2/2h$ in the energy range of 800-8000 cm^{-1} (0.1 – 1 eV) [78]. This seemingly odd result agrees in fact with the calculations based on the tight-binding model [78]. Nevertheless, the interlayer coupling is essential for the observations of a number of interesting effects such as a 3D-1D crossover in high magnetic field [8, 123]. The previous infrared measurements on graphite [8, 78, 124] were all based on reflectivity measurements and the Kramers-Kronig (KK) analysis that relies on extrapolations beyond the cut-off of the actual data and thus introduces a certain systematic inaccuracy to the resulting conductivity. In order to improve the reliability it is desirable to measure the optical conductivity directly.

In section 7.2, we employ a combination of infrared ellipsometry and reflectance measurements of cleaved HOPG samples that allows us to investigate the full optical conductivity tensor, namely both ab plane and c axis conductivity without the recourse to Kramers-Kronig_analysis. Our data confirm that the sheet optical conductivity of graphite is close to the universal conductivity $\pi e^2/2h$ of intrinsic graphene in the mid-IR region. Moreover, these measurements have placed certain constraints on the c-axis optical conductivity without taking any optical data on a surface containing the c-axis

that is hard to prepare and which properties are severely effected by polishing [125, 126].

In section 7.3, we carried out systematic study of bulk graphite in the quantum limit. Intense magnetic fields can radically alter properties of materials and produce a myriad of novel effects and novel states of matter [26, 87, 127]. One intriguing example is the field-induced transformation expected in an anisotropic three-dimensional (3D) metal. Provided only the lowest Landau levels (LLs) are populated (a condition referred to as the quantum limit), coherent charge motion in the direction perpendicular to the magnetic field is arrested. Therefore magnetic field initiates a crossover from 3D to 1D transport along the direction of the field [128]. A suitable candidate system to exhibit this phenomenon is graphite. In this anisotropic semimetal comprised of weakly coupled graphene sheets, a combination of low carrier density and small effective masses allows one to achieve the quantum limit condition in fairly modest magnetic fields along the c-axis (7-8T) [119]. A manifestation of the 3D to 1D crossover is the field dependence of the relaxation rate $1/\tau$ associated with the lowest LLs [128]. This fundamental electronic characteristic is difficult to infer from transport studies but can be directly probed via infrared (IR) spectroscopy.

Here, via IR spectroscopy of graphite we probe lifetimes τ associated with the lowest LLs in the quantum limit with field perpendicular to the graphene planes. We find that $1/\tau \propto B$ for the lowest LLs, which is distinct from power laws typically found in other classes of low dimensional systems[26] but consistent with the hypothesis of a 3D to 1D crossover [128]. Empowered by the experimental data for lifetimes, we were

able to elucidate the anomalous linear magneto-resistance in samples of weakly interacting graphene sheets. This peculiar form of magneto-resistance was discovered nearly 40 years ago in bulk graphite [119, 129] and recently observed in mesoscopic samples comprised of only few graphene layers [130, 131].

7.2 Zero field optical conductivity of graphite by infrared ellipsometry and reflectance

We studied two large (6X6 mm^2) HOPG samples of XYA grade (c-axis misorientation less than 0.4^o) from different suppliers. Ellipsometry measurements in the energy range 400 to 6000 cm^{-1} (0.05 – 0.75 eV) were performed at room temperature using an ellipsometer by Woollam Inc. coupled to Bruker IFS-66vs IR interferometer. Ellipsometric coefficients Ψ and Δ were measured at three angles of incidence: 45, 60 and 75 degrees, where $e^{i\Delta}\tan\Psi = r_p/r_s$. Here, r_p and r_s are reflectance coefficients for the light polarized parallel (p-polarization) and perpendicular (s-polarization) to the plane of incidence, respectively. Near-normal incidence reflectance was measured in the range of 15 to 25,000 cm^{-1} (0.018 – 3.1 eV).

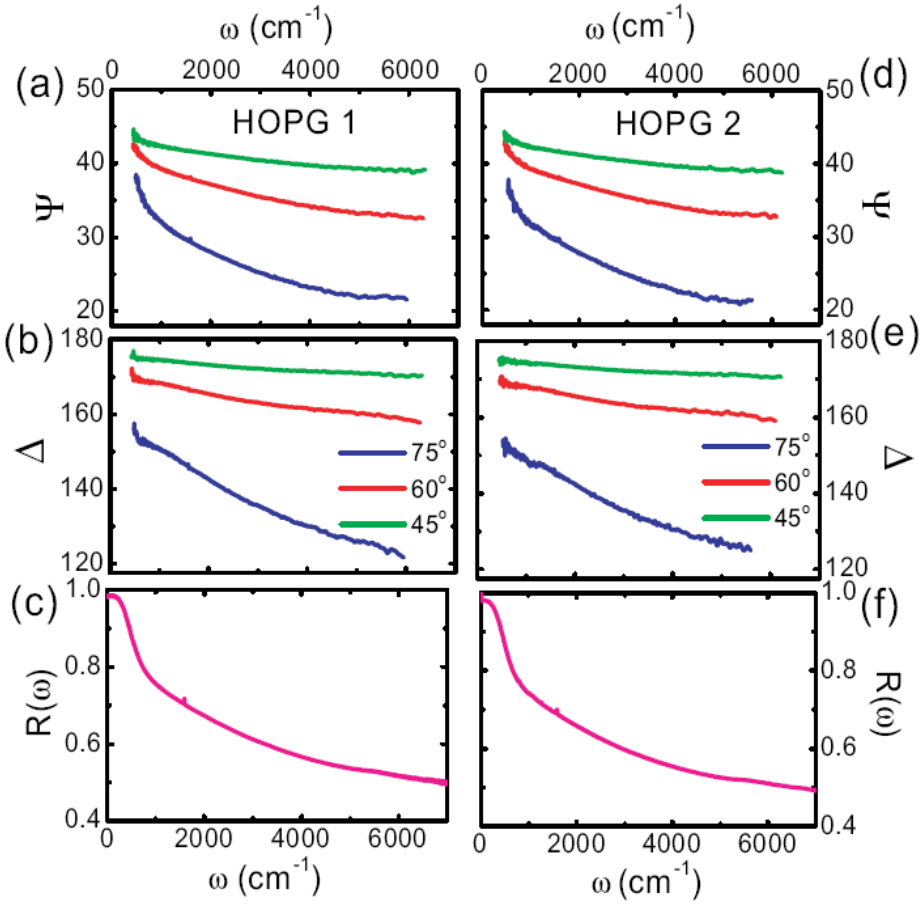

Figure 7.1: Ellipsometric coefficients Ψ and Δ of sample HOPG1 (panel (a) and (b)) and HOPG2 (panel (d) and (e)) for three incident angels. Panel (c) and (f): the reflectance spectra for HOPG1 and HOPG2.

Figure 7.1 depicts ellipsometry and reflectivity data. The Ψ and Δ curves for these two samples are very similar. Because graphite is anisotropic, the ellipsometric coefficients Ψ and Δ are determined by both the ab plane and c axis optical conductivity $\sigma(\omega)=\sigma_1(\omega)+i\sigma_2(\omega)$ [57]. In principle, both the ab plane and c axis optical conductivity can be inferred from ellipsometric measurements carried out at multiple incident angles [57] at each given frequency. However, this is difficult to achieve in practice for most

anisotropic samples. Consider the pseudo-dielectric function at a given angle of incidence that is governed both $\sigma^{ab}(\omega)$ and $\sigma^{c}(\omega)$. In practice, the two unknown components of the conductivity tensor can be extracted only if the pseudo-dielectric functions are different at different incident angles. Unfortunately, in the case of the graphite the measured pseudo-dielectric functions at different incident angles are very close to each other, and measurements at multiple angles of incidence provide only limited extra information compared to one measurement at a single angle. Therefore, it is hard to determine $\sigma^{ab}(\omega)$ and $\sigma^{c}(\omega)$ simultaneously through the usual analysis of ellipsometry data collected for the ab-plane surfaces.

In order to make the data inversion more reliable, we employed a causality consistent procedure to analyze both the ellipsometry and reflectance data [20]. Since the data taken on the ab-surface are more sensitive to the ab-plane components of the dielectric tensor, both real and imaginary parts of $\sigma^{ab}(\omega)$ were varied independently in every experimental frequency point. For the c-axis optical conductivity that affects less the measured data, we use a smooth KK consistent parameterization as a trial function, namely a Drude-Lorentz model with limited number of oscillators. We then allowed both the ab plane and c-axis conductivity to vary to fit the ellipsometry and reflectance data [20]. When a good fit was found, we varied the c-axis trial function and repeated the fitting procedure. After trying a large number of c-axis functions, we find that when an acceptable fit of the raw data is achieved (taking into account the error bars), the resulting $\sigma_1(\omega)$ spectra for ab plane and c-axis always fall into the shaded areas in Fig 7.2(a) and 7.2(b), respectively. We conclude that a combination of the ellipsometry and

reflectance data indicates that the ab plane and c axis optical conductivity are within the shaded areas in Fig 7.2(a) and 7.2(b), respectively. Similar results were found for both HOPG samples.

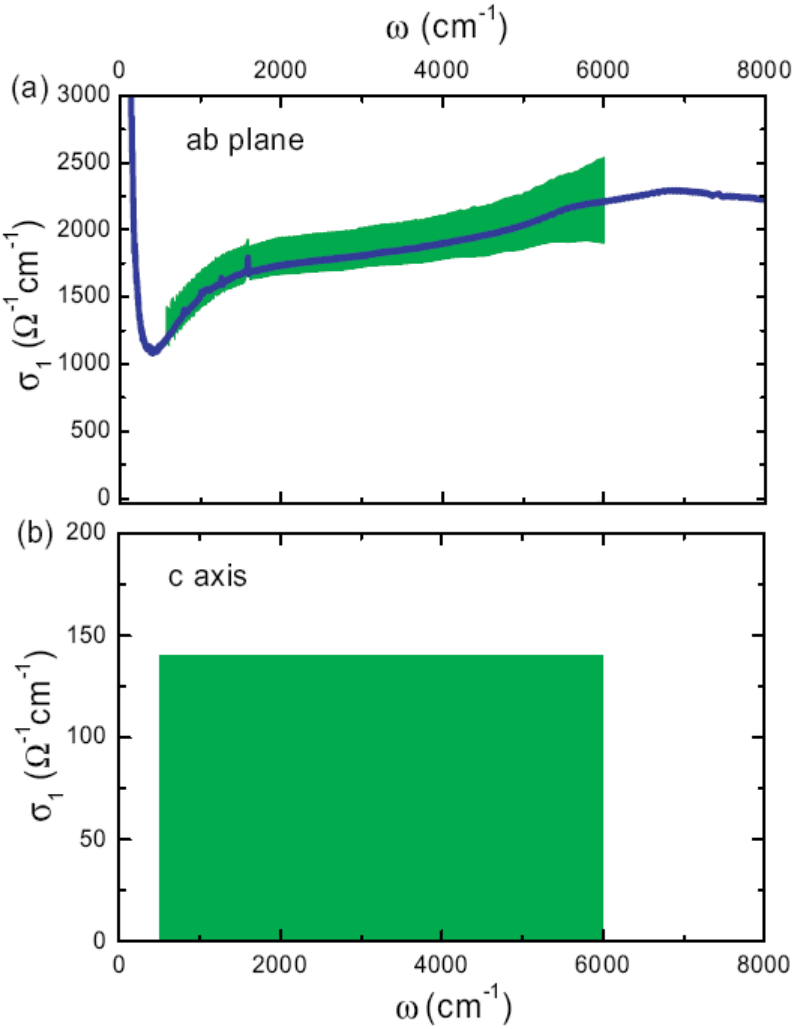

Figure 7.2: (a) Solid curve, ab plane conductivity obtained from Kramers-Kronig transformation of the reflectance data. Shaded area: the range of ab plane conductivity extracted from a causality consistent modeling of the raw data in Fig 7.1, as detailed in the text. (b) Shaded area: the range of c-axis conductivity.

The range of the real part of the sheet optical conductivity $G_1(\omega)$ for the HOPG samples are shown in Fig. 7.3, where $G_1(\omega) = \sigma_1^{ab}(\omega)*d$ and d=3.35A is the interlayer spacing. The $G_1(\omega)$ spectra are in good agreement with results reported in [78]. The $G_1(\omega) = \pi e^2/2h \tanh(\omega/4T)$ spectrum for intrinsic graphene at T = 300K is also shown in Fig. 7.3 for comparison. The suppression of $G_1(\omega)$ of graphene at 300K with respect to the universal conductivity $\pi e^2/2h$ in the low frequency region is due to thermal effects. Our measurements provide a direct confirmation that the sheet optical conductivity of bulk graphite is close to the universal conductivity of intrinsic graphene $\pi e^2/2h$ in the mid-IR range. This interesting observation is consistent with calculations of sheet optical conductivity within the Slonczewski-McClure-Weiss model [78] and calculations based on a multilayer graphene model [115]. Interestingly, the conductivity of graphite does not show a resonance peak around the interlayer coupling energy as observed in bilayer [7]. Previous calculation [78]has shown that the conductivity for a particular k_z value indeed shows strong resonance peaks similar to bilayer, but the resonance features are averaged out in the k_z integrated total conductivity. This effect is due to the continuous changing of the band splitting from a maximum value (0.9 eV for the conduction band and 0.7 eV for the valence band) at the K point to zero at the H point. The enhancement of $G_1(\omega)$ in graphite at higher energies with respect to the universal conductivity stems from the interband transitions near the K point of the band structure, where the band is characterized by a van Hove singularity [78].

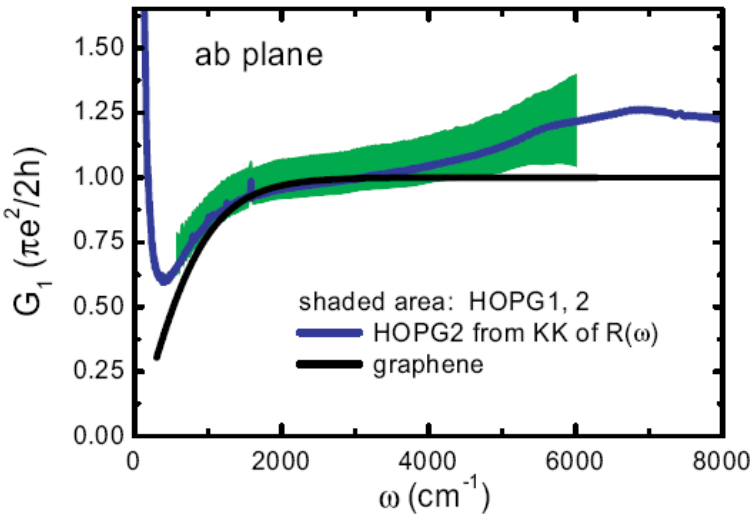

Figure 7.3: The sheet optical conductivity of graphite (the optical conductivity per graphene layer) $G_1(\omega)$ spectra obtained from a causality consistent modeling of ellipsometry and reflectance data, together with $G_1(\omega)$ spectrum of sample HOPG2 extracted from KK of reflectance data. The theoretical $G_1(\omega)$ spectrum for graphene at 300K is also shown for comparison.

While the experimental uncertainty of the in-plane optical conductivity (shaded area in Fig. 7.2a) is about 10-15%, the relative spread of the allowed c-axis conductivity compatible with this set of experimental data is notably larger (shaded area in Fig. 7.2b). The c axis dielectric function ε_1 from our fitting also has large uncertainties, ranging from 2 to 8 in the mid-IR. These uncertainties are due to the insensitivity of the ab plane measurements on the c axis optical constants as discussed above. On the other hand, it is very challenging to measure the c-axis conductivity from samples with ac surface due to issues such as surface roughness, polishing, and leakage of the ab plane component. Consequently, the c-axis optical constants in the literature show a large spread [125, 126, 132, 133]. Our study placed constraints on the range of the c-axis conductivity

from measurements of ab surface samples without the aforementioned complications associated with the ac surface. Interestingly, the c-axis optical constants in the literature [125, 126, 132, 133] all fall into the range inferred from our study. Recent theoretical calculations of the c-axis conductivity [115] also place the theoretical spectrum within the constraints that we have identified here. Further work is needed to accurately determine the c-axis conductivity and explore the interlayer coupling in graphite.

In summary, we carried out systematic IR reflectance and ellipsometric measurements on HOPG. These experiments have allowed us to determine model-independently both the ab plane and c-axis optical conductivity, although the inaccuracy of the latter one remain significant. We verified that the sheet optical conductivity $G_1(\omega)$ of HOPG is close to the universal conductivity of intrinsic graphene $\pi e^2/2h$ in the mid-IR range, which is consistent with recent theoretical calculations.

7.3 Infrared probe of the anomalous magnetotransport of highly oriented pyrolytic graphite in the extreme quantum limit

HOPG samples were measured in zero field as described in section 7.2. The magneto-reflectance $R(\omega,B)$ were measured in the Faraday geometry: **E** vector in the graphene plane and magnetic field **B** parallel to the c axis of the sample. Our in-house apparatus enables absolute measurements of $R(\omega,B)$ in fields up to 8T over a broad

frequency range (15 to 4,000 cm^{-1}) [134]. Data in selected magnetic fields were acquired using a sub-THz Martin-Puplett interferometer and extend down to 7 cm^{-1}. The magneto-reflectance ratios R(ω,B)/R(ω,B=0) in the range 20-3,000 cm^{-1} with B=7-18 T were obtained at the National High Magnetic Field Laboratory in Tallahassee. All data in magnetic field were taken at 5K.

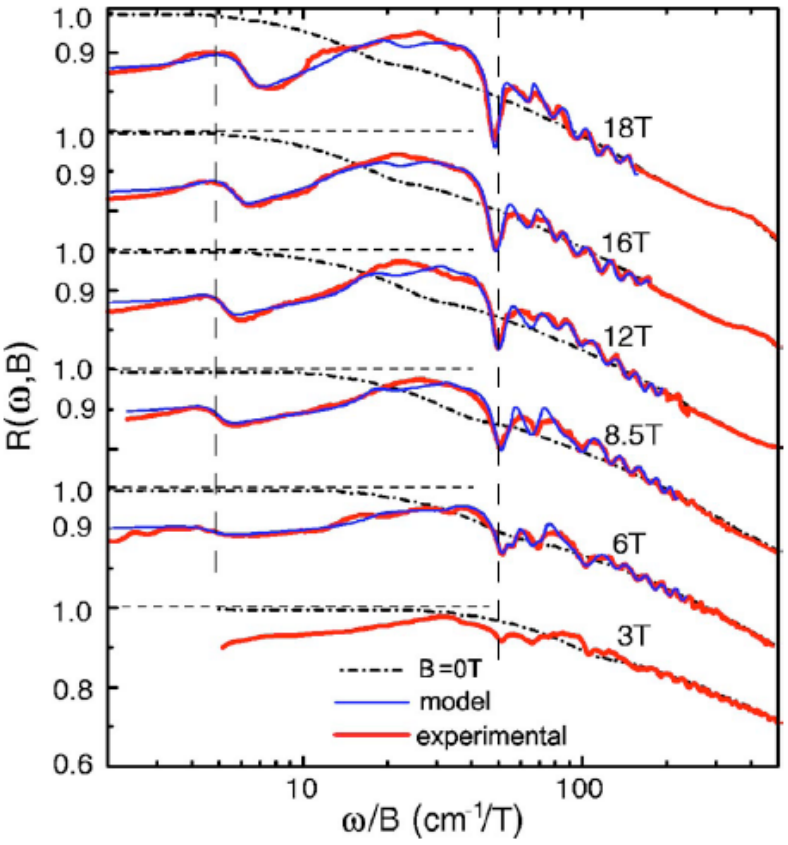

Figure 7.4: The ω/B scaled plot of the *ab*-plane reflectance spectra R(ω,B) in several magnetic fields. At each field *B*, the zero field reflectance spectrum R(ω,B=0) is also scaled by the corresponding factor *B* for comparison. Every set of spectra is offset by 30% for clarity. The model spectra are obtained from the analysis detailed in the text.

Insights into the anomalous magneto-transport can be provided by a systematic investigation of magneto-reflectance R(ω,B) spectra, which are displayed in a ω/B scaled plot in Fig. 7.4. To highlight field-induced changes of the optical properties, at each field B the zero field reflectance spectrum R(ω,B=0) is also scaled by the same factor B and shown together with R(ω,B) for comparison. Two new features are observed in the high-field spectra: i) the reflectance at low frequency is strongly suppressed and no longer extrapolates to unity in the DC limit; ii) the R(ω,B) spectra reveal a series of field-dependent resonances extending up to 3,000 cm^{-1} (see also the bottom panel of Fig. 7.5). The dramatic suppression of the low frequency reflectance R(ω □0 ,B) is an IR counterpart of the enormous positive magnetoresistance of graphite exceeding 1000 in 18T field [119]. The resonance features in R(ω,B) originate from the inter-LL transitions. An inspection of Fig. 7.4 shows that the frequencies of the strongest resonances reveal a linear dependence on magnetic field.

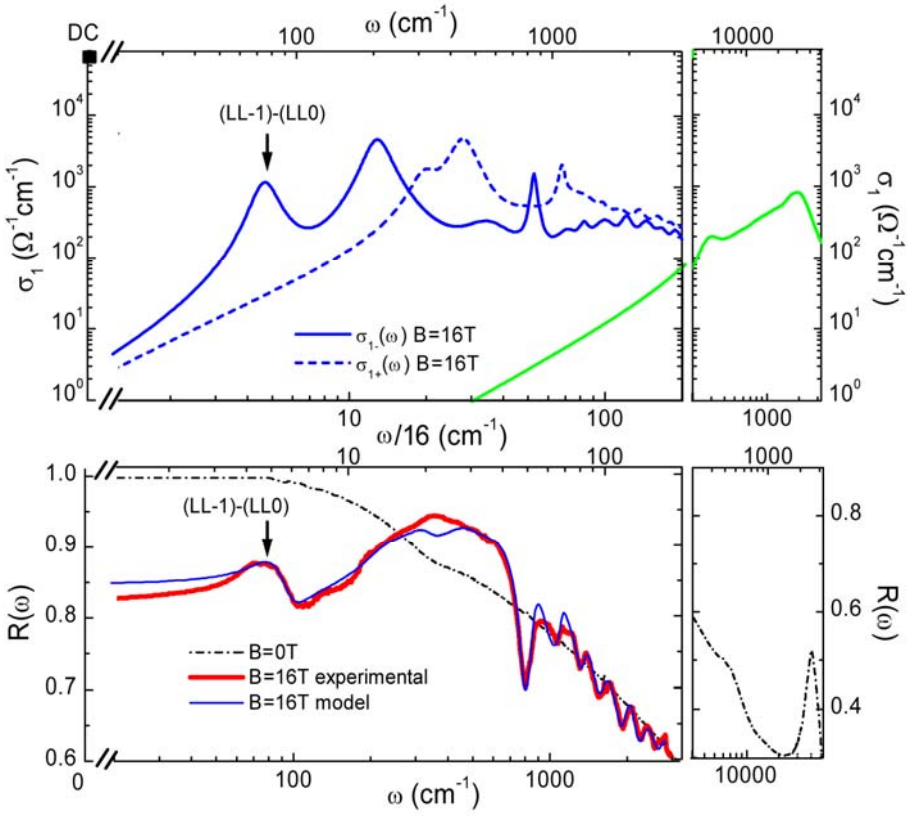

Figure 7.5: Top panel: model spectra $\sigma_{1+}(\omega)$ and $\sigma_{1-}(\omega)$ at 16 T obtained from the analysis detailed in the text. The black square on the left axis represents the dc conductivity σ_{dc} at 0 T. The green curve is the high frequency field-independent absorption in both $\sigma_{1+}(\omega)$ and $\sigma_{1-}(\omega)$. Bottom panel: experimental R(ω) spectra at 0 and 16 T and model spectra R(ω) at 16 T. The arrows indicate the resonance features in R(ω) and $\sigma_{1-}(\omega)$ due to the (LL-1)-(LL0) transition.

The rather complicated form of the R(ω,B) spectra and its systematic evolution with magnetic field are both in accord with the SWMC band theory of HOPG. To show this we analyzed R(ω,B) spectra displayed in Fig. 7.4 using a magneto-optical Lorentzian model for the complex conductivity due to inter-LL transitions $\sigma_{\pm}^{LL}(\omega)$ [135]:

$$\sigma_{\pm}^{LL}(\omega) = \sum_{j} \frac{\omega_{pj\pm}^{2}}{4\pi} \frac{\omega}{\omega/\tau_{j\pm} + i(\omega_{j\pm}^{2} - \omega^{2})} \quad (7.3.1)$$

This equation yields a series of resonance peaks at ω_{j+} and ω_{j-} at the poles of the left- and right-hand circularly polarized conductivity $\sigma_{\pm}^{LL}(\omega)$. Each peak is defined through the linewidth $1/\tau_{j\pm}$ and the oscillator strength $\omega_{pj\pm}^{2}$. Inter-LL transitions at both K and H points of the Brillouin zone [136, 137] are included in our fitting. According to SWMC theory, more than a dozen inter-LL transitions are likely to contribute to R(ω,B) in the studied frequency range. However, the parameters in Eq. (7.3.1) are strictly constrained by both the analytical properties of $\sigma_{\pm}(\omega)$ and the selection rules of inter-LL transitions [119, 137]. Following these constraints, Eq. (7.3.1) is used to construct $\sigma_{\pm}(\omega)$, which are then used to evaluate the reflectance spectra $R(\omega)=[R_{+}(\omega)+R_{-}(\omega)]/2$. In addition, several field-independent Lorentzian oscillators are employed in both $\sigma_{1\pm}(\omega)$ to account for the absorption above 3,000 cm^{-1}, as displayed by the green (light gray) curve in Fig. 7.5. We observed an additional resonance feature in R(ω,B) below 8.5T in the range 50-100 cm^{-1}/T in Fig. 7.4, which is an expected consequence of the quantum limit [138]. The resonances in R(ω,B) below and above 8.5T are roughly at the same positions in the ω/B plot, with small deviations in the high frequency resonances. The two different sets of magneto-optical oscillators at $\omega_{j\pm}/B$ employed to fit experimental R(ω,B) are summarized in table 7.1. We use the transition energies from ref [137] to account for the inter-LL transitions at the H point. These transitions at the H point are at much higher energy compared to those at the K point and constitute a broad

background in R(ω,B) spectra [137]. We stress that all field-dependent oscillators employed in our model can be assigned to the inter-LL transitions at K and H points within the conventional SWMC band model [119].

The model spectra at representative fields obtained from the above analysis are depicted in Fig. 7.4 and 7.5. Both the peak structures and their field dependence in experimental R(ω,B) spectra are reproduced by our analysis. Of special interest is the lowest inter-LL transition (LL-1)-(LL0) shown in Fig. 7.6. This transition is well separated from higher energy resonances, therefore the reflectance in the vicinity of this mode is hardly affected by other higher energy modes in our model, which allows us to extract the parameters for this particular transition from the above analysis. Moreover, in the quantum limit LL-1 and LL0 are the only occupied levels [119], which are directly related to the magneto-transport properties. Therefore, special attention will be given to the (LL-1)-(LL0) transition. Both the resonance frequency of this transition and its linewidth $1/\tau$ follow a linear field dependence as shown in Fig. 7.6. This is evident from a close inspection of the experimental R(ω,B) spectra in Fig. 7.4. The power law of $1/\tau(B)$ below 6T field is yet to be explored, because at low fields the (LL-1)-(LL0) transition occurs at low energies beyond our detection limit.

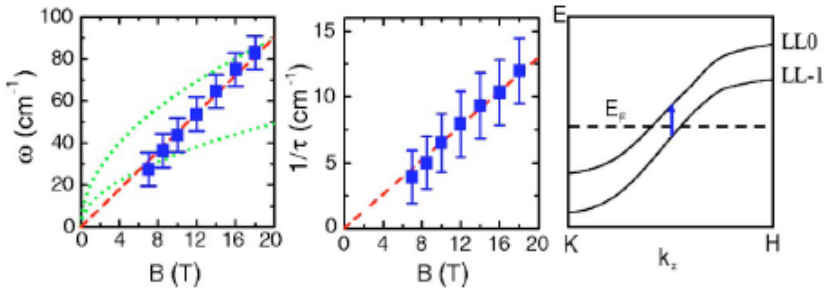

Figure 7.6: Resonance frequency (left panel) and linewidth (middle panel) of the (LL-1)-(LL0) transition in magnetic field. The dashed curves in these two panels are linear fits to the data. The dotted curves in the left panel are sqrt(B) fits. Right panel: a schematic of the LL-1 and LL0 Landau levels in the quantum limit.

Our magneto-reflectance data are in accord with the conventional SWMC band model of graphite [119]. In the SWMC model, the inter-LL transitions at K and H points have different field dependence: transitions at the K point reveal "normal" quasiparticle behavior (linear B scaling) [119], whereas transitions at the H point show Dirac behavior at high fields (~sqrt(B) scaling) [137]. Inter-LL transitions at both K and H points of the Brillouin zone are needed to fully account for our results on HOPG, which is consistent with previous magneto-optical study of bulk graphite samples [137].

We now show that the observed $1/\tau \propto B$ dependence for the (LL-1)-(LL0) transition (Fig. 7.6) is consistent with the notion of 3D to 1D crossover in an anisotropic 3D metal in the quantum limit [128]. The $1/\tau \propto B$ behavior in Fig. 7.6 most likely originates from the linear field dependence of the broadening of both LL-1 and LL0 [139], which is the scattering rate of the quasiparticles. In the quantum limit, the carriers have finite momentum only along the field direction (c-axis) and move diffusively in the transverse direction (ab plane) when scattered by impurities. The carrier-impurity scattering rate $1/\tau$ in the quantum limit is given by $1/\tau(B) = 2\pi n_0 u_0^2 v_B$ [128], where the

density of neutral impurities n_0 and impurity potential u_0 are B-independent. The 3D density of states v_B increases linearly with B in the quantum limit in graphite [119], giving rise to the linear B dependence of $1/\tau$. The increase of $1/\tau$ by a factor of 3 from 6T to 18T is consistent with a threefold increase of v_B in this range [119]. The interactions between carriers can give additional corrections to $1/\tau$ (B), which have weak logarithmic field dependence [140]. Therefore our data for the field dependence of the relaxation rate are in accord with the specific prediction of a model involving 3D to 1D crossover in the quantum limit.

Based on the observed $1/\tau \propto$ B result, we propose an explanation for the anomalous linear magneto-resistance found both in mesoscopic graphite systems [130, 131] and in bulk graphite [119]. First, the giant positive magneto-resistance of graphite is clearly related to the electronic spectral weight transfer of the Drude mode in the B=0 spectrum to finite energies in magnetic field (Fig. 7.5). The spectral weight transfer results in a drastic suppression of the conductivity in the DC limit by more than 10^3. Data in Figs. 7.4, 7.5 furthermore show that the lowest energy electronic excitation in the quantum limit is the (LL-1)-(LL0) transition revealing the linear field dependence of the relaxation rate. Let us explore the consequences of these findings for magneto-resistance that we will analyze following the standard form appropriate for the quantum limit as shown in:[128, 141]

$$\rho_{xx} = \frac{\rho_1\rho_2(\rho_1+\rho_2)+(\rho_1\boldsymbol{R}_2^2+\rho_2\boldsymbol{R}_1^2)\boldsymbol{B}^2}{(\rho_1+\rho_2)^2+(\boldsymbol{R}_1+\boldsymbol{R}_2)^2\boldsymbol{B}^2} \quad (7.3.2)$$

where ρ_{xx} is the ab-plane resistivity, ρ_i and $\boldsymbol{R_i = 1/n_i q_i}$ are the resistivity and Hall coefficient of the electrons (i=1) and holes (i=2), and n_i and q_i are the density and charge of the carriers. Note that in the quantum limit the off-diagonal term in the resistivity tensor can still be expressed as R_iB as shown in Ref. [128]. We emphasize that here Eq. (7.3.2) is not the semiclassical magnetoresistance: it follows from a fully quantum mechanical treatment, and ρ_i and $\boldsymbol{R_i}$ are B-dependent quantities. At high fields, the B^2 term dominates over the zero field term in the numerator, therefore the latter can be neglected. In the quantum limit, transport in the ab plane is diffusive with ρ_i given by $\boldsymbol{1/\rho_i \sim e^2 \nu_B D}$ [140] where $\boldsymbol{D \sim l_B^2/\tau}$ is the diffusion coefficient and $\boldsymbol{l_B \sim 1/\sqrt{eB}}$ is the magnetic length. From $\boldsymbol{\nu_B} \propto$ B [119], and D~1 ($1/\tau \propto$ B from our results), we obtain $1/\rho_i \propto$ B. Because the net carrier density in the sample n_1-n_2 is constant at high field [119] and $n_1 \sim n_2 \propto$ B, we obtain $\boldsymbol{(R_1 + R_2)B \propto 1/B}$. This expression is valid in the magnetic field regime where graphite shows linear magneto-resistance. In even higher field, n_1-n_2 decreases with field due to the so-called magnetic freeze-out effect, and correspondingly a saturation of magneto-resistance is observed. Combined with $\boldsymbol{R_i = 1/n_i e} \propto 1/B$, we find $\rho_{xx} \propto$ B. Therefore, our study suggests that the anomalous linear magneto-resistance of graphite originates from quantum transport in magnetic field. The above analysis can also be used to account for the linear magneto-resistance in mesoscopic graphite-based electronic systems [130, 131], where interlayer coupling between graphene sheets is important.

The use of a two-band model in our analysis is corroborated by a recent study of mesoscopic graphite field-effect transistors [130, 131], which shows that the slope of

the magneto-resistance can be tuned by changing the carrier compensation n_e-n_h consistent with Eq (7.3.2). Previously, a model based on magnetic-field-dependent scattering range of ionized impurity scattering [129] was proposed to explain the linear magneto-resistance in graphite. Due to the field-dependent screening of charged impurities, the scattering rate in this model has a field dependence of $1/\tau \sim B/(c+B)^2$, where c is a constant [129]. This prediction is in contrast to our observation $1/\tau \propto B$. Therefore, our study shows that impurities in graphite are likely to be uncharged and the ionized impurity scattering model [129] may not be applicable. Indeed, previous magneto-transport studies have shown the limitations of the ionized impurity model [142, 143]. Recently, an interesting model based on Dirac fermions [144] is proposed to account for linear magneto-resistance in graphite. However, our studies of HOPG have clearly demonstrated that Dirac fermions do not play a dominant role in the magneto-transport in graphite.

In summary, we carried out systematic IR magneto-optical experiments on HOPG. We show that the optical properties of HOPG in both zero field and magnetic fields can be understood within the conventional SWMC band theory of graphite. We observed an unconventional linear field dependence of the inverse lifetime $1/\tau$ associated with the lowest LLs. This observation is consistent with the hypothesis of 3D to 1D crossover in an anisotropic 3D metal in the quantum limit [128]. This new result has allowed us to address the origin of the anomalous linear magneto-resistance in mesoscopic graphite-based electronic systems [130, 131] as well as in bulk graphite [119]. Our work has demonstrated the potential of IR spectroscopy for the study of LL dynamics and novel magneto-transport phenomena in carbon based materials such as

mesoscopic graphite and graphene [75, 96], which are directly related to the novel functionalities of magneto-electronic devices based on these materials.

Table 7.1: The magneto-optical Lorentzian oscillators used in the analysis of R(ω,B) and their possible assignments. ω_+/B and ω_-/B in (cm^{-1}/T) are frequencies (normalized by magnetic field *B*) of the oscillators in $\sigma_+(\omega)$ and $\sigma_-(\omega)$, respectively, used to account for the inter-Landau-level (LL) transitions at *K* point. Two sets of oscillators are used in two field ranges: (*h*) $B>8.5$ T and (*l*) $B\leq 8.5$ T. The theoretical transition frequencies are labeled following Nakao's notation [136]: *hn-em* refers to the transition from the *n*th hole LL to the *m*th electron LL, etc. The transitions *e*1-*e*8 and *e*1-*e*9 are allowed only below the quantum limit. The last eight columns list $\omega_{j\pm}$ and $1/\tau_{j\pm}$ (both in cm^{-1}) used for the model spectrum R(ω) at 16 and 8.5 T. The parameters of the oscillator used for $m^+=0,-1$ transitions at *H* point are 16 T: $\omega_0=1212$ cm^{-1}, $\omega_p=4243$ cm^{-1}, $1/\tau=500$ cm^{-1}; 8.5 T: $\omega_0=818$ cm^{-1}, $\omega_p=3211$ cm^{-1}, $1/\tau=300$ cm^{-1}.

ω_-^h/B	ω_-^l/B	Theory	Assignment	ω_+^h/B	ω_+^l/B	Theory	Assignment	$\omega_{pj-}^{16\ T}$	$\omega_{pj+}^{16\ T}$	$1/\tau_{j-}^{16\ T}$	$1/\tau_{j+}^{16\ T}$	$\omega_{pj-}^{8.5\ T}$	$\omega_{pj+}^{8.5\ T}$	$1/\tau_{j-}^{8.5\ T}$	$1/\tau_{j+}^{8.5\ T}$
4.6	4.3	4.5	(LL-1)-(LL0)	19.7	19.3	22	(LL-1)-*e*1	1238	2265	10	40	725	1347	6	24
13	18	17	(LL0)-*e*1	28	33	35	(LL0)-*e*2	4016	5578	29	60	3683	4953	5	10
35	35	32	*h*2-(LL0)	50	50	49	*h*2-*e*1	2079	2377	167	227	2325	2629	96	128
54		54	*h*1-*e*2	69		70	*h*1-*e*3	2082	2349	26	33				
	58	58	*h*3-*e*1		73	70	(LL-1)-*e*4					1959	2130	7	9
70	61	66	(LL0)-*e*4	85	76	76	*h*3-*e*2	1538	1672	146	175	1581	1753	36	45
						81	(LL0)-*e*5								
83	80	84	*h*2-*e*3	98	95	98	*h*2-*e*4	1056	1143	67	78	2340	2519	92	108
		85	*h*4-*e*2			101	*h*4-*e*3								
100		99	*h*1-*e*5	115		113	*h*1-*e*6	2461	2615	210	240				
	111	105	*e*1-*e*8		126	119	*e*1-*e*9					2158	2293	70	79
		107	*h*3-*e*4			121	*h*3-*e*5								
		110	*h*5-*e*3			124	*h*5-*e*4								
122		127	*h*2-*e*6	137		141	*h*2-*e*7	1874	1977	128	143				
		130	*h*4-*e*5			144	*h*4-*e*6								
	141	141	*h*1-*e*8		156	155	*h*1-*e*9					2213	2324	73	80
145		149	*h*3-*e*7	160		163	*h*3-*e*8	2305	2409	211	232				
		153	*h*5-*e*6			167	*h*5-*e*7								
	164	169	*h*2-*e*9		179	183	*h*2-*e*10					2343	2442	101	110
167		172	*h*4-*e*8	182		186	*h*4-*e*9	1498	1559	172	187				
		175	*h*6-*e*7			189	*h*6-*e*8								

Acknowledgements: This chapter contains materials in Z.Q. Li, S.-W. Tsai, W.J. Padilla, S.V. Dordevic, K.S. Burch, Y.J. Wang, and D.N. Basov, "*Infrared probe of the anomalous magnetotransport of highly oriented pyrolytic graphite in the extreme quantum limit*", Phys. Rev. B 74, 195404 (2006). The dissertation author was the primary investigator and author of this paper. The coauthors of this paper all contribute to the studies describe in this chapter.

Bibliography

[1] C. H. Ahn, A. Bhattacharya, M. D. Ventra, J. N. Eckstein, C. D. Frisbie, M. E. Gershenson, A. M. Goldman, I. H. Inoue, J. Mannhart, J. M. Andrew, F. M. Alberto, N. Douglas, and T. Jean-Marc, Rev. Mod. Phys. **78**, 1185 (2006).

[2] C. H. Ahn, J. M. Triscone, and J. Mannhart, Nature **424**, 1015 (2003).

[3] Z. Q. Li, G. M. Wang, K. J. Mikolaitis, D. Moses, A. J. Heeger, and D. N. Basov, Appl. Phys. Lett. **86**, 223506 (2005).

[4] Z. Q. Li, G. M. Wang, N. Sai, D. Moses, M. C. Martin, M. Di Ventra, A. J. Heeger, and D. N. Basov, Nano Lett **6**, 224 (2006).

[5] Z. Q. Li, V. Podzorov, N. Sai, M. C. Martin, M. E. Gershenson, M. D. Ventra, and D. N. Basov, Phys. Rev. Lett. **99**, 016403 (2007).

[6] Z. Q. Li, E. A. Henriksen, Z. Jiang, Z. Hao, M. C. Martin, P. Kim, H. L. Stormer, and D. N. Basov, Nat Phys **4**, 532 (2008).

[7] Z. Q. Li, E. A. Henriksen, Z. Jiang, Z. Hao, M. C. Martin, P. Kim, H. L. Stormer, and D. N. Basov, arXiv:0807.3776. (2008).

[8] Z. Q. Li, S. W. Tsai, W. J. Padilla, S. V. Dordevic, K. S. Burch, Y. J. Wang, and D. N. Basov, Phys. Rev. B **74**, 195404 (2006).

[9] G. D. Wilk, R. M. Wallace, and J. M. Anthony, J. Appl. Phys. **89**, 5243 (2001).

[10] W. Cochran, Adv. Phys. **9**, 387 (1960).

[11] A. K. Tagantsev, V. O. Sherman, K. F. Astafiev, J. Venkatesh, and N. Setter, J. Electroceram. 11, 5 (2003).

[12] M. G. Harrison, D. Fichou, F. Garnier, and A. Yassar, Opt. Mater.9, 53 (1998).

[13] P. J. Brown, H. Sirringhaus, M. Harrison, M. Shkunov, and R. H. Friend, Phys. Rev. B **63**, 125204 (2001).

[14] K. E. Ziemelis, A. T. Hussain, D. D. C. Bradley, R. H. Friend, J. Rühe, and G. Wegner, Phys. Rev. Lett. **66**, 2231 (1991).

[15] G. Wang, D. Moses, A. J. Heeger, H.-M. Zhang, M. Narasimhan, and R. E. Demaray, J. Appl. Phys. **95**, 316 (2004).

[16] L. Burgi, R. H. Friend, and H. Sirringhaus, Appl. Phys. Lett. **82**, 1482 (2003).

[17] C. Lee, P. Ghosez, and X. Gonze, Phys. Rev. B **50**, 13379 (1994).

[18] M. Mikami, S. Nakamura, O. Kitao, and H. Arakawa, Phys. Rev. B **66**, 155213 (2002).

[19] E. J. Singley, K. S. Burch, R. Kawakami, J. Stephens, D. D. Awschalom, and D. N. Basov, Phys. Rev. B **68**, 165204 (2003).

[20] A. B. Kuzmenko, Rev. Sci. Instrum. **76**, 083108 (2005).

[21] G. A. Samara, and P. S. Peercy, Phys. Rev. B **7**, 1131 (1973).

[22] P. A. Fleury, and J. M. Worlock, Phys. Rev. **174**, 613 ((1968)).

[23] I. A. Akimov, A. A. Sirenko, A. M. Clark, J. H. Hao, and X. X. Xi, Phys. Rev. Lett. **84**, 4625 (2000).

[24] R. H. Lyddane, R. G. Sachs, and E. Teller, Phys. Rev. 59, 673 (1941).

[25] J. G. Traylor, H. G. Smith, R. M. Nicklow, and M. K. Wilkinson, Phys. Rev. B 3, 3457 (1971).

[26] T. Ando, A. B. Fowler, and F. Stern, Rev. Mod. Phys. **54**, 437 (1982).

[27] M. Di Ventra, S. Evoy, and R. Heflin, *Introduction to Nanoscale Science and Technology* (Kluwer Academic Publishers: Dordrecht, 2004).

[28] C. D. Dimitrakopoulos, and P. R. L. Malenfant, Adv. Mat. **14**, 99 (2002).

[29] E. S. Snow, J. P. Novak, P. M. Campbell, and D. Park, Appl. Phys. Lett. **82**, 2145 (2003).

[30] C. Joachim, J. K. Gimzewski, and A. Aviram, Nature **408**, 541 (2000).

[31] Di Ventra, M.; Zwolak, M. DNA electronics in Encyclopedia of Nanoscience and Nanotechnolog, Vol. 2, p. 475. H. S. Nalwa ed. American Scientific Publishers, 2004.

[32] H. Sirringhaus, P. J. Brown, R. H. Friend, M. M. Nielsen, K. Bechgaard, B. M. W. Langeveld-Voss, A. J. H. Spiering, R. A. J. Janssen, E. W. Meijer, P. Herwig, and D. M. de Leeuw, Nature **401**, 685 (1999).

[33] B. H. Hamadani, and D. Natelson, Appl. Phys. Lett. **84**, 443 (2004).

[34] G. Wang, J. Swensen, D. Moses, and A. J. Heeger, J. Appl. Phys. **93**, 6137 (2003).

[35] S. M. Sze, *Physics of Semiconductor Devices* (Wiley: New York, 1981).

[36] T. Li, J. W. Balk, P. P. Ruden, I. H. Campbell, and D. L. Smith, J. Appl. Phys. **91**, 4312 (2002).

[37] Y. H. Kim, D. Spiegel, S. Hotta, and A. J. Heeger, Phys. Rev. B **38**, 5490 (1988).

[38] M. V. Fischetti, D. A. Neumayer, and E. A. Cartier, J. Appl. Phys. **90**, 4587 (2001).

[39] A. J. Heeger, S. Kivelson, J. R. Schrieffer, and W. P. Su, Rev. Mod. Phys. **60**, 781 (1988).

[40] R. Österbacka, X. M. Jiang, C. P. An, B. Horovitz, and Z. V. Vardeny, Phys. Rev. Lett. **88**, 226401 (2002).

[41] B. Horovitz, Solid State Commun. **41**, 729 (1982).

[42] B. Horovitz, R. Österbacka, and Z. V. Vardeny, Synthetic Metals **141**, 179 (2004).

[43] S. Kivelson, and A. J. Heeger, Phys. Rev. Lett. **55**, 308 (1985).

[44] A. D. Meyertholen, Z. Q. Li, D. N. Basov, M. M. Fogler, M. C. Martin, G. M. Wang, A. S. Dhoot, D. Moses, and A. J. Heeger, Appl. Phys. Lett. **90**, 222108 (2007).

[45] N. Sai, Z. Q. Li, M. C. Martin, D. N. Basov, and M. Di Ventra, Phys. Rev. B **75**, 045307 (2007).

[46] R. G. Endres, D. L. Cox, and R. R. P. Singh, Rev. Mod. Phys. **76**, 195 (2004).

[47] A. Omerzu, M. Licer, T. Mertelj, V. V. Kabanov, and D. Mihailovic, Phys. Rev. Lett. **93**, 218101 (2004).

[48] G. Malliaras, and R. H. Friend, Phys. Today 58, No. 5, 53 (2005).

[49] S. R. Forrest, Nature **428**, 911 (2004).

[50] E. Silinsh, and V. Cápek, *Organic molecular crystals : interaction, localization, and transport phenomena* (American Institute of Physics, New York, 1994).

[51] M. Pope, and C. E. Swenberg, *Electronic processes in organic crystals and polymers* (Oxford University Press, New York, 1999), pp. xxix.

[52] M. E. Gershenson, V. Podzorov, and A. F. Morpurgo, Rev. Mod. Phys. **78**, 973 (2006).

[53] R. W. I. d. Boer, M. E. Gershenson, A. F. Morpurgo, and V. Podzoro, Phys. Stat. Solid. **201**, 1302 (2004).

[54] V. Podzorov, E. Menard, A. Borissov, V. Kiryukhin, J. A. Rogers, and M. E. Gershenson, Phys. Rev. Lett. **93**, 086602 (2004).

[55] V. Podzorov, E. Menard, J. A. Rogers, and M. E. Gershenson, Phys. Rev. Lett. **95**, 226601 (2005).

[56] M. Fischer, M. Dressel, B. Gompf, A. K. Tripathi, and J. Pflaum, Appl. Phys. Lett. **89**, 182103 (2006).

[57] R. M. A. Azzam, and N. M. Bashara, *Ellipsometry and polarized light* (Elsevier North-Holland, Amsterdam ; New York, New York, 1977), pp. xvii.

[58] D. C. Tsui, S. J. Allen, R. A. Logan, A. Kamgar, and S. N. Coppersmith, Surface Science **73**, 419 (1978).

[59] N. F. Mott, and M. Kaveh, Adv. Phys. **34**, 329 (1985).

[60] F. Wooten, *Optical Properties of Solids* (Academic, New York, London, 1972).

[61] A. D. Becke, Phy. Rev. A **38**, 3098 (1988).

[62] C. Lee, W. Yang, and R. G. Parr, Phys. Rev. B **37**, 785 (1988).

[63] We used the SOCORRO package for the calculations (http://dft.sandia.gov/Socorro/mainpage.html). Common density functionals such as the GGA used in this work do not account for van der Waals forces, which determine the correct distance between molecules. However, when the bonding distances are fixed at the experimental ones, this deficiency has negligible effect on the electronic dispersion that is mainly determined by the overlap of the electronic wave functions.

[64] D. Kafer, and G. Witte, Phys. Chem. Chem. Phys. **7**, 2850 (2005).

[65] E. Menard, A. Marchenko, V. Podzorov, M. E. Gershenson, D. Fichou, and J. A. Rogers, Adv. Mat. **18**, 1552 (2006).

[66] A. Troisi, and G. Orlandi, Phys. Rev. Lett. **96**, 086601 (2006).

[67] K. P. Pernstich, B. Rossner, and B. Batlogg, Nat Mater **7**, 321 (2008).

[68] P. R. Wallace, Physical Review **71**, 622 (1947).

[69] G. W. Semenoff, Phys. Rev. Lett. **53**, 2449 (1984).

[70] K. S. Novoselov, A. K. Geim, S. V. Morozov, D. Jiang, M. I. Katsnelson, I. V. Grigorieva, S. V. Dubonos, and A. A. Firsov, Nature **438**, 197 (2005).

[71] Y. Zhang, J. W. Tan, H. L. Stormer, and P. Kim, Nature **438**, 201 (2005).

[72] Z. Jiang, E. A. Henriksen, L. C. Tung, Y. J. Wang, M. E. Schwartz, M. Y. Han, P. Kim, and H. L. Stormer, Phys. Rev. Lett. **98**, 197403 (2007).

[73] R. S. Deacon, K. C. Chuang, R. J. Nicholas, K. S. Novoselov, and A. K. Geim, Phys. Rev. B **76**, 081406 (2007).

[74] T. Ando, Y. Zheng, and H. Suzuura, J. Phys. Soc. Jpn. **71**, 1318 (2002).

[75] N. M. R. Peres, F. Guinea, and A. H. Castro Neto, Phys. Rev. B **73**, 125411 (2006).

[76] V. P. Gusynin, and S. G. Sharapov, Phys. Rev. B **73**, 245411 (2006).

[77] R. R. Nair, P. Blake, A. N. Grigorenko, K. S. Novoselov, T. J. Booth, T. Stauber, N. M. R. Peres, and A. K. Geim, Science **320**, 1308 (2008).

[78] A. B. Kuzmenko, E. van Heumen, F. Carbone, and D. van der Marel, Phys. Rev. Lett. **100**, 117401 (2008).

[79] N. M. R. Peres, T. Stauber, and A. H. Castro Neto, <http://arxiv.org/abs/0709.1163> (2007).

[80] J. Martin, N. Akerman, G. Ulbricht, T. Lohmann, J. H. Smet, K. von Klitzing, and A. Yacoby, Nat Phys **4**, 144 (2008).

[81] M. M. Qazilbash, M. Brehm, B.-G. Chae, P. C. Ho, G. O. Andreev, B.-J. Kim, S. J. Yun, A. V. Balatsky, M. B. Maple, F. Keilmann, H.-T. Kim, and D. N. Basov, Science **318**, 1750 (2007).

[82] A. H. Castro Neto, F. Guinea, N. M. R. Peres, K. S. Novoselov, and A. K. Geim, <http://arxiv.org/abs/0709.1163> (2007).

[83] J. Gonzalez, F. Guinea, and M. A. H. Vozmediano, Phys. Rev. Lett. **77**, 3589 (1996).

[84] E. H. Hwang, B. Y. K. Hu, and S. Das Sarma, Phys. Rev. B **76**, 115434 (2007).

[85] C. H. Park, F. Giustino, M. L. Cohen, and S. G. Louie, Phys. Rev. Lett. **99**, 086804 (2007).

[86] D. N. Basov, E. J. Singley, and S. V. Dordevic, Phys. Rev. B **65**, 054516 (2002).

[87] D. N. Basov, and T. Timusk, Rev. Mod. Phys. **77**, 721 (2005).

[88] L. Degiorgi, Rev. Mod. Phys. **71**, 687 (1999).

[89] J. Gonzalez, F. Guinea, and M. A. H. Vozmediano, Phys. Rev. B **59**, R2474 (1999).

[90] S. Das Sarma, E. H. Hwang, and W. K. Tse, Phys. Rev. B **75**, 121406 (2007).

[91] S. Y. Zhou, G. H. Gweon, J. Graf, A. V. Fedorov, C. D. Spataru, R. D. Diehl, Y. Kopelevich, D. H. Lee, S. G. Louie, and A. Lanzara, Nat Phys **2**, 595 (2006).

[92] A. Bostwick, T. Ohta, T. Seyller, K. Horn, and E. Rotenberg, Nat. Phys. **3**, 36 (2006).

[93] S. Y. Zhou, G. H. Gweon, A. V. Fedorov, P. N. First, W. A. de Heer, D. H. Lee, F. Guinea, A. H. Castro Neto, and A. Lanzara, Nat Mater **6**, 770 (2007).

[94] F. Wang, Y. Zhang, C. Tian, C. Girit, A. Zettl, M. Crommie, and Y. R. Shen, Science **320**, 206 (2008).

[95] S. A. Mikhailov, and K. Ziegler, Phys. Rev. Lett. **99**, 016803 (2007).

[96] V. P. Gusynin, S. G. Sharapov, and J. P. Carbotte, Phys. Rev. Lett. **96**, 256802 (2006).

[97] A. K. Geim, and A. H. MacDonald, Phys. Today 60, 35 (2007).

[98] A. K. Geim, and K. S. Novoselov, Nat. Mater. 6, 183 (2007).

[99] K. S. Novoselov, E. McCann, S. V. Morozov, V. I. Fal/'ko, M. I. Katsnelson, U. Zeitler, D. Jiang, F. Schedin, and A. K. Geim, Nat Phys **2**, 177 (2006).

[100] J. Nilsson, A. H. C. Neto, N. M. R. Peres, and F. Guinea, Phys. Rev. B **73**, 214418 (2006).

[101] T. Stauber, N. M. R. Peres, F. Guinea, and A. H. C. Neto, Phys. Rev. B **75**, 115425 (2007).

[102] E. V. Castro, K. S. Novoselov, S. V. Morozov, N. M. R. Peres, J. M. B. L. dos Santos, J. Nilsson, F. Guinea, A. K. Geim, and A. H. C. Neto, Phys. Rev. Lett. **99**, 216802 (2007).

[103] T. Ohta, A. Bostwick, T. Seyller, K. Horn, and E. Rotenberg, Science **313**, 951 (2006).

[104] E. McCann, Phys. Rev. B **74**, 161403 (2006).

[105] E. McCann, and V. I. Fal'ko, Phys. Rev. Lett. **96**, 086805 (2006).

[106] F. Guinea, A. H. C. Neto, and N. M. R. Peres, Phys. Rev. B **73**, 245426 (2006).

[107] J. Nilsson, A. H. C. Neto, F. Guinea, and N. M. R. Peres, Phys. Rev. B **76**, 165416 (2007).

[108] H. Min, B. Sahu, S. K. Banerjee, and A. H. MacDonald, Phys. Rev. B **75**, 155115 (2007).

[109] E. A. Henriksen, Z. Jiang, L. C. Tung, M. E. Schwartz, M. Takita, Y. J. Wang, P. Kim, and H. L. Stormer, Phys. Rev. Lett. **100**, 087403 (2008).

[110] S. V. Kusminskiy, D. K. Campbell, and A. H. C. Neto, arXiv:cond-mat/0805.0305.

[111] J. Yan, E. A. Henriksen, P. Kim, and A. Pinczuk, arXiv:cond-mat/0712.3879.

[112] L. M. Malard, J. Nilsson, D. C. Elias, J. C. Brant, F. Plentz, E. S. Alves, A. H. C. Neto, and M. A. Pimenta, Phys. Rev. B **76**, 201401 (2007).

[113] A. B. Kuzmenko, unpublished.

[114] J. Nilsson, A. H. C. Neto, F. Guinea, and N. M. R. Peres, Phys. Rev. Lett. **97**, 266801 (2006).

[115] J. Nilsson, A. H. C. Neto, F. Guinea, and N. M. R. Peres, Phys. Rev. B **78**, 045405 (2008).

[116] E. J. Nicol, and J. P. Carbotte, Phys. Rev. B **77**, 155409 (2008).

[117] D. S. L. Abergel, and V. I. Fal'ko, Phys. Rev. B **75**, 155430 (2007).

[118] L. M. Zhang, Z. Q. Li, D. N. Basov, M. M. Fogler, Z. Hao, and M. C. Martin, arXiv:0809.1898

[119] N. B. Brandt, S. M. Chudinov, and Y. G. Ponomarev, *Semimetals 1. Graphite and its compounds.* (North-Holland ;, Amsterdam, 1988), p. v.

[120] The gap formula in (E. McCann, Phys. Rev. B 74, 161403 (2006)) did not take into account Delta_AB and v4. However, we find that finite Delta_AB and v4 values have no effect on the gap. Specifically, Delta_AB primarily modifies the E1 and E4 bands, while leaving unchanged the gap between the E2 and E3 bands at k=0, as shown in Fig 2(a). In addition, v4 always appears in a term v4*k in the Hamiltonian (Phys. Rev. B 78, 045405 (2008)), therefore it has zero effect on the gap.

[121] In the calculation of the energy bands Ei(k) (i=1,2,3,4), we used the approximation Delta=0, which can be justified for the purpose of estimating e2 and e3. The gap Delta is very small (<80 meV) in the voltage range studied in our work, and does not affect the higher energy bands E1(k=0) or E4(k=0) and

therefore the value of e2. Note that Delta=0 is only assumed when calculating Ei(k), but not in the Delta term in the expression of e2. Moreover, E2 and E3 bands are modified by the gap only at energies below\Delta/2. Because EF is much larger than Delta/2 under applied voltage (E. McCann, Phys. Rev. B 74, 161403(R) (2006)), E2(k=k_F)and E3(k=k_F) are not affected by Delta. Therefore, a finite gap does not modify the value of e3 compared to that with Delta=0.

[122] L. A. Falkovsky, and A. A. Varlamov, European Physical Journal B **56**, 281 (2007).

[123] A. F. Hebard., unpublished.

[124] E. A. Taft, and H. R. Philipp, Phys. Rev. 138, 197 (1964).

[125] H. Venghaus, Phys. Stat. Sol. (b) 81, 221 (1977).

[126] M. Zanini, D. Grubisic, and J. E. Fischer, Phys. Stat. Sol. (b) 90, 151 (1978).

[127] S. D. Sarma, and A. Pinczuk, *Perspectives in quantum Hall effects : novel quantum liquids in low-dimensional semiconductor structures* (Wiley, New York, 1997), pp. xiv.

[128] A. A. Abrikosov, Sov. Phys. JETP 29, 746 (1969).

[129] J. W. McClure, and W. J. Spry, Physical Review **165**, 809 (1968).

[130] Y. Zhang, J. P. Small, M. E. S. Amori, and P. Kim, Phys. Rev. Lett. **94**, 176803 (2005).

[131] S. V. Morozov, K. S. Novoselov, F. Schedin, D. Jiang, A. A. Firsov, and A. K. Geim, Phys. Rev. B **72**, 201401 (2005).

[132] D. L. Greenaway, G. Harbeke, F. Bassani, and E. Tosatti, Physical Review **178**, 1340 (1969).

[133] J. G. E. Jellison, J. D. Hunn, and H. N. Lee, Phys. Rev. B **76**, 085125 (2007).

[134] W. J. Padilla, Z. Q. Li, K. S. Burch, Y. S. Lee, K. J. Mikolaitis, and D. N. Basov, Rev. Sci. Instrum. **75**, 4710 (2004).

[135] B. Lax and J. G. Mavroides, in Semiconductors and Semimetals Vol. 3, edited by R. K. Willardson and A. C. Beer (Academic Press, New York and London, 1967), pp. 321–401.

[136] K. Nakao, J. Phys. Soc. Jpn. 40, 761 (1976).

[137] W. W. Toy, M. S. Dresselhaus, and G. Dresselhaus, Phys. Rev. B **15**, 4077 (1977).

[138] The different resonance features below and in the quantum limit can be attributed to the different allowed inter-LL transitions in these two ranges. For instance, the inter-LL transitions such as e1-e8 and e1-e9 are only allowed below the quantum limit, as detailed in Table 1.

[139] In 2D systems under strong magnetic field, the resonance linewidth of the inter-LL transition coincides with the broadening of the corresponding LLs, provided impurity scattering is the dominant relaxation process.

[140] S.-W. Tsai, D. L. Maslov, and L. I. Glazman, Physica B: Condensed Matter **312-313**, 586 (2002).

[141] N. W. Ashcroft, and N. D. Mermin, *Solid state physics* (Holt, New York,, 1976), pp. xxi.

[142] Y. Iye, P. M. Tedrow, G. Timp, M. Shayegan, M. S. Dresselhaus, G. Dresselhaus, A. Furukawa, and S. Tanuma, Phys. Rev. B **25**, 5478 (1982).

[143] Y. Iye, L. E. McNeil, and G. Dresselhaus, Phys. Rev. B **30**, 7009 (1984).

[144] A. A. Abrikosov, Phys. Rev. B **60**, 4231 (1999).